IOP Publishing J. Phys.: Condens. Matter 38 (2026) 235901 https://doi.org/10.1088/1361-648X/ae74a8

Journal of Physics: Condensed Matter

OPEN ACCESS

RECEIVED
2 March 2026

REVISED
14 May 2026

ACCEPTED FOR PUBLICATION
28 May 2026

PUBLISHED
11 June 2026

PAPER

Electronic contribution of Frenkel defects to thermal conductivity in body centred cubic transition metals from first-principles study

J Singh[1,2,3], D Nguyen-Manh[3,4,*], A Mottura[2] and B Cai[2,*]

[1] EPSRC Centre for Doctoral Training in Topological Design, The University of Birmingham, Birmingham, United Kingdom
[2] School of Metallurgy and Materials, The University of Birmingham, Birmingham B15 2TT, United Kingdom
[3] Materials Division, United Kingdom Atomic Energy Authority, Culham Campus, Abingdon OX14 3DB, United Kingdom
[4] Department of Materials, The University of Oxford, Oxford OX1 3PH, United Kingdom
[*] Authors to whom any correspondence should be addressed.

E-mail: duc.nguyen@ukaea.uk and b.cai@bham.ac.uk

Keywords: Frenkel pairs, Fermi velocity, electron scattering time, *s*-*d* scattering correction, thermal conductivity, *Ab-Initio*

Abstract

Body centred cubic (BCC) transition metals are of high interest for nuclear applications, where they are subject to high radiation damage, which causes the material's properties to decay. Measuring the electrical and thermal properties of these materials after irradiation poses challenges due to sample size, activity, and cost of running the experiments. Traditional methods of measuring thermal properties require bulk samples. Newer measuring techniques were developed for smaller samples, but they have their limitations. Therefore, a new First Principles' method was developed to predict the electronic thermal conductivity and resistivity of Frenkel pairs (FP) in BCC transition metals. The Boltzmann Transport equation for the thermal conductivity requires the electron heat capacity, the Fermi velocity, and the electron scattering time. A model to calculate the electron-FP scattering time for point defects is shown, and extended to include the electron–phonon contributions. The electron–phonon corrections of *s*-electron to the *d*-band from the Mott model for transition metals are presented and discussed. The method presented in this work can provide an initial insight, in the degradation of the electric and thermal properties of irradiated transition metals and their alloys, including high entropy alloys.

1. Introduction

Thermal conductivity is dominated by two mechanisms, electron and lattice (phonon) scatterings. In particular, electrons dominate the heat transfer mechanism in metals, especially in $d-$block transition metals, where the additional $d-$electrons and the metallic bonds provide high mobility to the electrons [1]. Electrons transfer heat by scattering, the electrons moving in the metal will scatter at other particles and quasi particles, like impurities, phonons, and to a lesser degree, other electrons [1, 2]. These scatterings will impede the movement of the electrons, hence causing them to lose energies due to the changes in the velocity. Impurities can be quite different, from elemental impurities, to point defects, like a missing ion in the lattice, to self-interstitial, all provide a centralized scattering centre [1], and can be treated in the same way. Of high interest are vacancies and self-interstitial pairs, known also as Frenkel pairs (FP). FP are defects that are formed during irradiation events in the ballistic phase [3]. Experimentally measuring the thermal conductivity of irradiated metals poses many issues due to the radioactivity of the samples, cost of the studies, and health and safety limitations. As such, developing a theoretical model to successfully calculate the thermal conductivity is crucial for material development and understanding how well a material will perform in a nuclear irradiation environment. Hence, the electronic thermal conductivity for a material can be calculated knowing the electron scattering time, its Fermi velocity, and the electronic heat capacity [1, 2].

There are different experimental methods to find the thermal properties of materials, resistivity measurements combined with Wiedemann–Franz law [4], laser flash analysis (LFA) [4–6], and newer methods like transient grating spectroscopy (TGS) measurements [7–10], or the 3-omega method [11–13]. All these methods can be used to accurately measure the thermal conductivity, but they all have restrictions, either on the size of the samples, its surface finish, and the cost of running them. LFA and resistivity measurements are more reliable on bulk samples. TGS is a powerful method, it can be used *in-situ* during irradiation experiments [7], and it can achieve small time resolutions [10]. However, it is restricted by the surface finish of the sample, and the probing depth of 2.5 to 8.5 μm [8, 9]. The 3-omega method can also be used on small samples, and wires, but it is limited by the need to deposit complex surfaces, and layering them on top of the sample to take the measurements [11–13]. The limiting factors remain, the sample size, irradiation experiment cost and duration, dose rate and activities, these limit the material testing and refinement for recent alloys. Therefore, it is significant to have a model that can accurately predict the changes in thermal conductivity following irradiation damage.

Computational methods like Green–Kubo [14, 15] integrate over time and correlate the lattice vibrations to calculate the thermal conductivity, or other properties like electrical conductivity. There are also non equilibrium molecular dynamics [16], which create a heat flux in an atomistic system to calculate the thermal conductivity. These are often limited by the complexity of the structures, and the simulation time lengths required. Mason [2, 17] developed a method to calculate the thermal conductivity from *Ab-Initio* and Molecular Dynamics simulations. The method produces accurate results, which relies on the fitting of the electron scattering time to experimental data, either by fitting the experimental resistivities [2], or with the thermal diffusivity obtained from TGS [8, 17]. This method limits the modelling to systems that have experimental data available, or for which that data can be acquired. Hence, it is difficult to test new alloys before manufacturing.

Other methods to calculate the thermal conductivity rely on the Boltzmann's transport equations (BTE) [1, 18]. In First Principles, the BTE can be simplified and used with the relaxation time approximation (RTA) [1, 18–20]. Smirnov [20] extended the BTE to account for electron scattering processes, and electron–phonon coupling, which allowed them to get a good comparison with experimental data. However, the scattering terms described by Smirnov were only considered in the x-direction due to the cubic symmetries of the elements considered in their study [20]. This would work only in pure, defect free, materials. The addition of defects is bound to break the symmetry, changing the electron scattering rate, and some of these defects will be direction-dependent, hence making the scattering rate dependent on the orientation of the defect. The use of RTA can lead to erroneous results as it does not consider the electronic configuration, which is fundamental, as electrons can only scatter in empty states which adhere to the Pauli exclusion principle [1]. Claes *et al* [21] have compared, analysed, and expanded RTA approximations, and shown that the results produced with RTA have to be carefully examined. Jayaraj *et al* [22] went further in developing a model that used the RTA model and fitted experimental data to find accurate conductivity results. This method works primarily because of the experimental fitting of the data, as it provides the information missed by the RTA.

The electron scattering time, also known as relaxation time, or collision time, is the average time between electron collisions with other particles and quasi-particles [1]. The inverse of the relaxation time is therefore the probability that the electron will scatter [1, 23]. In a perfect infinite lattice, the scattering time would be infinite, and therefore the scattering probability would be negligible [23]. As there are no perfect lattices, the electrons will scatter from impurities, phonons, and other electrons. Transition metals in the d-block are special because they have available states in the d-subshell for the electrons. Mott and Jones considered that conduction is primarily done by s-subshell electrons, and thus resistance in transition metals also arises from the scattering of s-electrons to the d-subshell [23]. The scattering probability should then be the sum between the scattering probability of the s-electrons with the impurity, and the d-electron on the impurity, while including the $s \rightarrow d$-shell scattering. This would also affect the electronic thermal conductivity that is directly proportional to the relaxation time. Hence, the larger the relaxation time, the larger the thermal conductivity.

In this work, a model was developed to study the effects of Frenkel defects in body centred cubic (BCC) transition metals. In the following sections, the methodology behind the first principles calculations is described. Then, the various parts that make up the model are introduced. Firstly, the Fermi velocity, the effective mass, and electronic thermal capacity are calculated. Then, a method to extract the perturbation potential from the difference of the perfect supercell and the supercells with defect is shown. From these, the FP resistivities are calculated and compared with the experimental available data. Furthermore, the electron–phonon contribution is approximated using the Kaganov model to increase the accuracy of the model. Additionally, using the Mott model the s-electrons to d-band scattering is accounted for in the electron–phonon model to understand the effects of the defects on the temperature dependence.

2. First-principles calculations

2.1. Computational details

The first principles simulations present in this work were performed using VASP 5.4 [24, 25], using semi-core Projector-Augmented-Wave Perdew–Burke–Ernzerhof generalized gradient approximation (GGA) [26] potentials for all elements. Semi-core electrons were included, the electrons used are shown in table 1. The structures used in this part were primitive structures with 1 atom, except in Cr where a conventional structure was used with 2 atoms. Because of this, the Cr pseudo-potential was duplicated to treat the atoms with the positive magnetic moment, and the negative magnetic moment as separate Cr species. This was done to have an atom with positive magnetic field and one with negative magnetic field to study the effects of the anti-ferromagnetism. Additionally, a magnetic field was applied to the Fe atom, and the calculations for Ta and W in their primitive structures were performed with spin orbit coupling. These simulations will be referred as primitive calculations. All the primitive calculations were performed with a plane-wave cut-off energy of 600 eV, the energy minimization was done with the Blocked-Davidson algorithm, and with an electronic convergence of 10^{-6} eV, using an additional support grid was enabled in the simulation to have a finer augmentation charge grid.

The structure optimization was performed with a force convergence of 10^{-5} eV Å^{-1}, using the conjugate gradient (CG) algorithm. The smearing algorithm used was the tetrahedron with Blöch corrections smearing with a $15 \times 15 \times 15$ K-mesh centred at Γ. In the case the simulations did not find the optimum structure in a run, the output structure was copied and used as the starting input for the next structure optimization. And, in the case that the optimization had reached a minimum but was not converging, the CG algorithm was changed to the 'Residual Minimization Method with Direct Inversion in the Iterative Subspace' (RMM-DIIS) algorithm, where the change step-size was determined from the previous simulations CG step-size multiplied by the 'trial-step' obtained from VASP. For W and Ta, an initial optimization was performed by letting the volume of the cell optimize, and using the resulting output structure as the input, the atomic position was optimized in the following simulation.

The self-consistent field (SCF) calculations were performed using the optimized structure, the smearing algorithm was the same as the structure optimization, tetrahedron with Blöch corrections, and using the same K-mesh of $15 \times 15 \times 15$ centred at Γ. The charge density produced in the SCF calculations was the basis for the following simulations.

Density of states (DOS) were calculated using the optimized structure, and the charge density from the SCF. The K-mesh was kept the same. A 0.1 eV DOS mesh was used.

The Fermi surface was calculated using the optimized structure, and the charge density from the SCF calculation. The K-mesh was increased from $15 \times 15 \times 15$ to $29 \times 29 \times 29$ centred at Γ. Meshes larger than the $29 \times 29 \times 29$ were not stable for all elements; hence, this mesh was chosen.

The band-structure calculations were performed using the 1st order Methfessel–Paxton (MP) smearing with a smearing factor of, $\sigma = 0.01$ eV, the optimized structure was used, and it also used the charge density from the SCF calculation. The high symmetry path was found using SeeK-Path [27, 28], and for BCC transition metals, this is $\Gamma \rightarrow H \rightarrow N \rightarrow \Gamma \rightarrow P \rightarrow H|P \rightarrow N$. The path was subdivided in 101 points, which resulted in 606 K-points. These results were post-processed using VASPKIT [29] and Python.

For the heat capacity, SCF simulations were performed using the optimized structure, the Fermi–Dirac smearing, with σ in ranges of 0.01 to 0.35 eV, which corresponds to an electron temperature range of 116 to 4061 K. The lower σ range was set at 0.01 eV as simulations below this value were not stable for all elements. Whereas, the upper range was set to be above the melting point of W, which is the highest across the BCC transition metals chosen in this work. The values of the energy at 0 K were extracted from the 0.01 eV simulations.

The perfect supercells were performed with a $5 \times 5 \times 5$ resulting in 250 atoms. As such, the K-mesh was reduced to $5 \times 5 \times 5$. The structure optimization was performed by optimizing both the volume and the atomic positions. The structures were optimized using the 1st order MP, with a smearing factor of $\sigma - 0.01$. The electronic minimization was performed using the 'FAST' algorithm in VASP, with the first ionic step using 12 electronic steps of Blocked-Davidson algorithm, and the rest using the RMM-DIIS algorithm. For Cr and Fe, the optimization was performed with the standard blocked-Davidson. The structure optimization algorithm used was CG. The convergence threshold was set to 10^{-3} eV Å^{-1}. The table 2, below, shows the optimized lattice constants and compares them with the experimental results. For the supercells with the defects, the optimized perfect supercell was taken and modified to include the defect as follows;

Table 1. Numbers of electrons chosen for the simulations.

Element	Periodic table element group old / new	# e$^-$	Valence electrons
V	VB / V	13	$3s^2 3p^6 4s^1 3d^4$
Nb			$4s^2 4p^6 5s^1 4d^4$
Ta			$5s^2 5p^6 5d^5$
Cr	VIB / VI	14	$3s^2 3p^6 4s^1 3d^5$
Mo			$4s^2 4p^6 5s^1 4d^5$
W			$5s^2 5p^6 6s^1 5d^5$
Fe	VIII	16	$3s^2 3p^6 4s^1 3d^7$

Table 2. Lattice parameter *a*, from perfect supercell structure optimization.

Element	Supercell dimensions (Å)	*a* (Å)	Experimental [18] (Å)
V	14.984 × 14.984 × 14.984	2.997	3.03
Nb	16.536 × 16.536 × 16.536	3.307	3.30
Ta	16.585 × 16.585 × 16.585	3.317	3.30
Cr	14.249 × 14.249 × 14.249	2.850	2.88
Mo	15.811 × 15.811 × 15.811	3.162	3.15
W	15.925 × 15.925 × 15.925	3.185	3.16
Fe	14.074 × 14.074 × 14.074	2.815	2.87

- for the vacancy, the central atom of the [111] string in the middle of the cell was deleted, resulting in a structure with 249 atoms.
- The dumbbell [111] dumbbell was created by replacing the centre atom along the [111] string with two atoms, which had a vector separation of $a \times [0.05, 0.05, 0.05]$ Å along the [111] dumbbell, where a is the lattice parameter. In Fe, the [110] dumbbell was created, which had a vector separation of $a \times [0.07, 0.07, 0]$ Å. These structures have 251 atoms.
- The crowdion structure was created for all elements except Fe. The crowdion was created by adding an atom at the centre of the cell, and displacing the other atoms in the [111] string following the kinklike static displacement field solution by Fitzgerald and Nguyen-Manh [30]. Which results in structures with 251 atoms.

These structures were then optimized by keeping the volume constant and only allowing the atomic positions to optimize. The method was otherwise similar to that described previously for the perfect supercell. In the case where the structure was close to the lowest energy state but was not converging with the CG algorithm, the algorithm was changed to the RMM-DIIS, where the change step-size was determined from the previous simulations CG step-size multiplied by the 'trial-step' obtained from VASP. The defect formation energies were calculated and compared with literature data to ensure that the defects were correct using the following equation,

$$H_f^{\text{defect}} = H_{\text{defect}} - \frac{n_{\text{defect}}}{n_{\text{perfect}}} H_{\text{perfect}} \tag{1}$$

where H_{defect}, and H_{perfect} are the total energies of the defect supercell and the energy of the perfect supercell from the converged structure optimization result, while the n_{defect}, and n_{perfect} are respectively the number of atoms in the defect supercell and perfect supercell.

The SCF simulations were all performed using the optimized structures, and the electronic minimization was changed to the blocked-Davidson algorithm, with the same K-mesh as the structure optimization.

The density of states simulations were performed by extending the SCF simulations, using the tetrahedron with Blöch corrections smearing with a step of 0.1 eV, the same K-mesh as the SCF calculations was used. VASPKIT [29] and Python were used to post-process the DOS results and decompose the DOS in the individual band contributions.

2.2. Fermi velocity and effective mass

The Fermi velocity can be calculated as [1],

$$\bar{v}_\mathrm{F} = \frac{1}{\hbar}\nabla_k E_\mathrm{F} \tag{2}$$

where, $\hbar$ is the reduced Planck constant, $\nabla_k E_\mathrm{F}$ is the gradient of the electron free energy as a function of K-wave vectors. In Python, the Fermi velocity was calculated by integrating over the Fermi surface using [2],

$$\bar{v}_\mathrm{F} = \frac{1}{\hbar}\sum_l \oint \left| \frac{\partial E_{k,l}}{\partial k} \cdot \underline{\hat{n}} \right| \mathrm{d}S \tag{3}$$

where l is the band index, and $\underline{\hat{n}}$ is the normal to the Fermi surface. The effective mass of electrons will be used in the electron–phonon scattering, but it is important to estimate correctly. The effective mass, m^* is defined as [1],

$$\frac{1}{m^*} = \frac{1}{\hbar^2}\frac{\partial^2 E}{\partial k_i \partial k_j} \tag{4}$$

from this, using band structure calculations along the high symmetry path, it is possible to extract the effective mass values from the bands that cross the Fermi surface. Only the value in between $-k_\mathrm{B}T_\mathrm{M} < \epsilon_\mathrm{F} < k_\mathrm{B}T_\mathrm{M}$ were used, where T_M is the melting temperature of the metal, and ϵ_F is the Fermi energy.

Using C2X [31] the VASP results were post-processed to produce a BXSF file, from which the bands that crossed the Fermi surface were determined and extracted using XCrySDen [32]. The code from Weinberg[5] [33], was used and modified for this work. The surface integral was performed using Einstein summation in the NumPy python library [34]. Furthermore, using a piecewise cubic spline the eigenvalues were interpolated from 29^3 to 116^3 using a marching cube algorithm method following the method used by Mason [2]. VASPKIT [29] was used to post-process the resulting band-structure simulations. The effective mass was averaged from the values obtained by the bands that crossed the Fermi surface.

Figure 1 shows the Fermi velocites overlaid on the Fermi surfaces of the BCC transition metals. While table 3 showcases the results obtained in this work, and compares the Fermi velocities with the work done by Mason [2] and Medjanik *et al* [35]. The results for Nb, Ta, and Cr mostly agree with Mason's work, while the others do not. However, the Fermi velocity for W, 7.53 Åfs^{-1}, does match with the experimental value of the electron hole velocity found by Medjanik *et al* of 7 Åfs^{-1}. These differences come down to the potentials used, in this work semi-core potentials with PBE-GGA were used for all the elements, while Mason used a semi-core HGH potential with LDA exchange correlation functional for W, and they lifted the spin degeneracy on Fe. The Cr Fermi velocity was calculated on a conventional cell to include the antiferromagnetic moments.

2.3. Electronic heat capacity from finite temperature approximation

To calculate the electronic thermal capacity, the Finite Temperature Approximation will be used. This approach relies on the properties of the Fermi–Dirac distribution to smear the electronic temperatures. The Fermi–Dirac distribution has the form of [24],

$$f(\epsilon) = \frac{1}{\exp\left[(\epsilon-\mu)/(k_\mathrm{B}T)\right]+1}. \tag{5}$$

The main reason the Fermi–Dirac smoothing function was chosen was due to the smearing factor $\sigma = k_\mathrm{B}T$, as it is related to the electronic temperature. Furthermore, at ground state, the energy changes are not small with changes in $f(\epsilon)$, hence, the free energy, F, is used [24],

$$F = E - \sum_{nk} w_k \sigma S(f_{nk}) \tag{6}$$

where w_k are weighting factors associated to a k-point k, and $S(f_{nk})$ is the entropy term and defined as,

$$S(f_{nk}) = -\left[f_{nk}\ln f_{nk} + (1-f_{nk})\ln(1-f_{nk})\right]. \tag{7}$$

---

[5] The version that was used and modified for this work corresponds to commit 781*b*3*ef*.

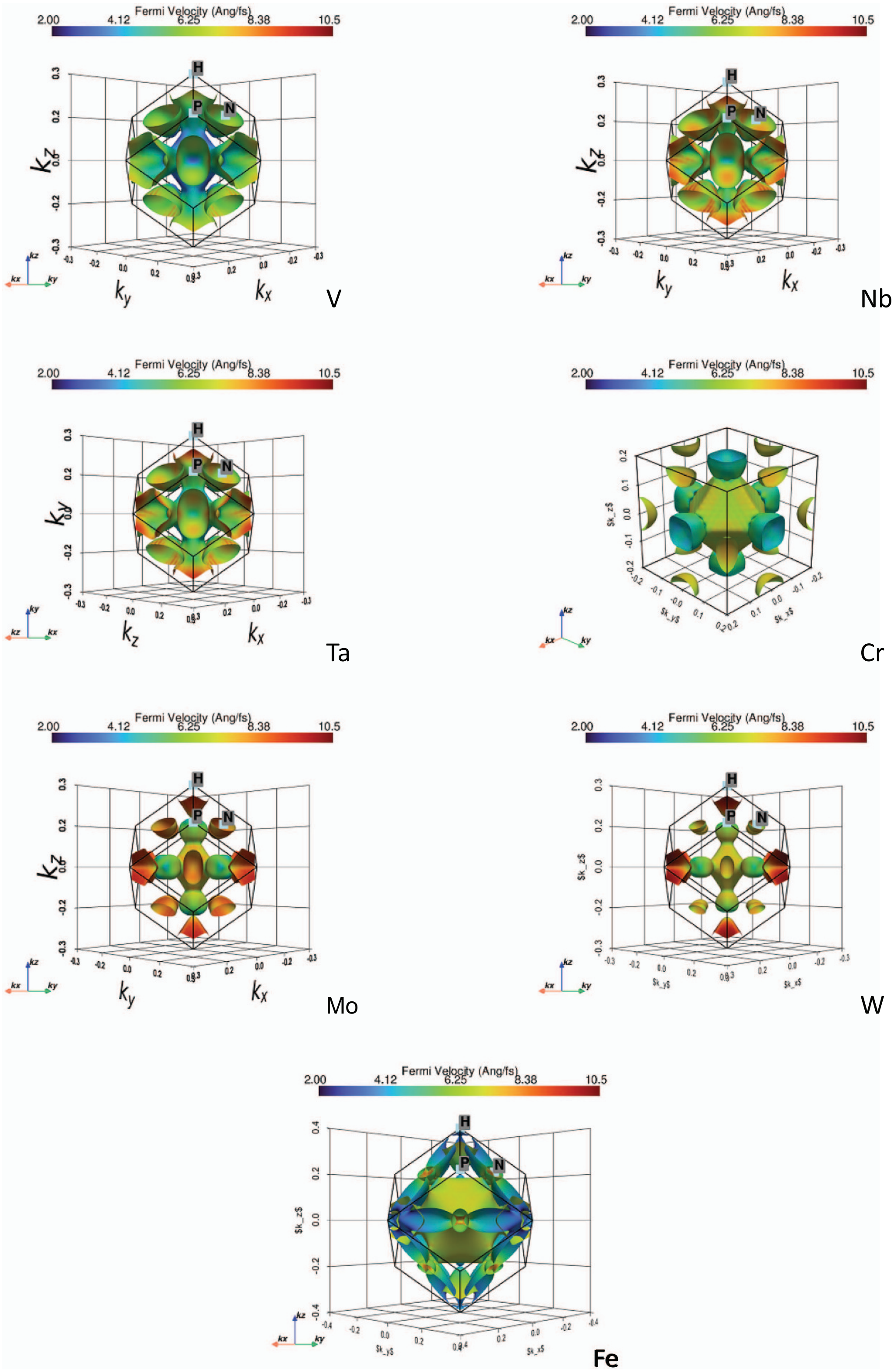

Figure 1. Fermi velocity of BCC transition metals in Åfs^{-1}. The Fermi surface of each element is overlaid with its Fermi velocity. Chromium Fermi surface is from the conventional cell to include the anti-ferromagnetic behaviour.

It becomes possible to calculate the heat capacity as equation (6) is in simpler terms [36],

$$F = U - TS \tag{8}$$

where U is the internal energy, T is the temperature and S the entropy. The first derivative in respect of temperature will result in,

Table 3. Effective mass and comparison of Fermi velocity of BCC transition metals.

Element	Effective mass ($\times 10^{-31}$ kg)	Fermi velocity (Åfs^{-1}) This work	Mason [2]	Medjanik *et al* [35]
V	3.02	5.41	4.47	
Nb	1.80	6.45	6.46	
Ta[1]	2.25	6.41	6.47	
Cr[2]	3.68	5.99	5.73	
Mo	1.15	7.45	8.72	
W[1]	1.42	7.53	9.50	7
Fe[3]	2.99	5.35	4.95	

[1] Non-collinear spin orbit coupling interaction included.

[2] Spin polarized anti-ferromagnetic, conventional cell.

[3] Spin polarized magnetic moments included.

$$S = -\frac{\mathrm{d}F}{\mathrm{d}T} \tag{9}$$

and the electronic thermal capacity is,

$$c_\mathrm{e} = T \times \frac{\mathrm{d}S}{\mathrm{d}T} = -T \times \frac{\mathrm{d}^2F}{\mathrm{d}T^2}. \tag{10}$$

The results obtained from equation (10) will be compared with the Sommerfeld model [1],

$$c_S = \frac{\pi^2}{3} k_\mathrm{B}^2 T g(\epsilon_\mathrm{F}) \tag{11}$$

where $g(\epsilon_\mathrm{F})$ is the value of the density of states at Fermi energy, which was determined from primitive cell DOS calculations. The results will also be compared with the Free electron gas solution (based on the Free electron model),

$$c_\mathrm{FE} = \frac{\pi^2}{2}\left(\frac{k_\mathrm{B}T}{\epsilon_\mathrm{F}}\right) n k_\mathrm{B} \tag{12}$$

where n is the number of free electrons, which has been taken to the number of electrons mentioned in table 1.

Using equation (10), the heat capacity for the BCC transition metals was calculated. For the thermal smearing at 0 K, the entropy should be 0 eV K^{-1}, this was considered when fitting the data to avoid numerical errors from differentiating. The data was fitted and interpolated to 1 K precision. The electronic heat capacity is in the 10^{-5} eV K^{-1} range, this is because unlike thermal conductivity, phonons are the dominating mechanism behind heat capacity, with electrons providing small additions to it. The results derived from equation (10) were compared with Sommerfeld approximation [1], with the values calculated from the Electron Free model. This comparison is shown in figure 2.

The results seem to showcase a common pattern for each element group. Group V starts close to the Sommerfeld and Free electron gas models at lower temperatures, and then start to diverge away at higher temperatures. Meanwhile, in group VI, the Sommerfeld model acts as a lower bound and the Free electron gas model as an upper bound, and the c_e calculated from First Principles simulations is contained between the two. The c_e calculated for Fe is larger than the two models, but after its Curie point it starts to diverge towards the approximations, and then diverge again at higher temperatures. The reason Cr and Fe look so differently at lower temperatures, is most likely due to the inclusion of the magnetic moments in the calculations. But at higher temperature, for Fe tend to converge close to the Free electron model solutions, while Cr keeps increasing. This is most likely due to the spin degeneracy in Fe and Cr, which is not accounted for in the Sommerfeld model, and as such does not provide accurate predictions of the electronic heat capacity. The results were also compared with linear experimental results from Tari [37]. The experimental values are larger in group V, but are close to group VI. Both Cr and Fe do not fully agree with the experimental results, and this deviation is most likely due to the inclusion of magnetic moments. There is an additional explanation for these differences; the results from Tari are from low-temperature experiments that have been extrapolated at higher temperature. Hence, some high-temperature contribution might have been ignored. But as the results are close to the same order of magnitude, they can be assumed to be correct.

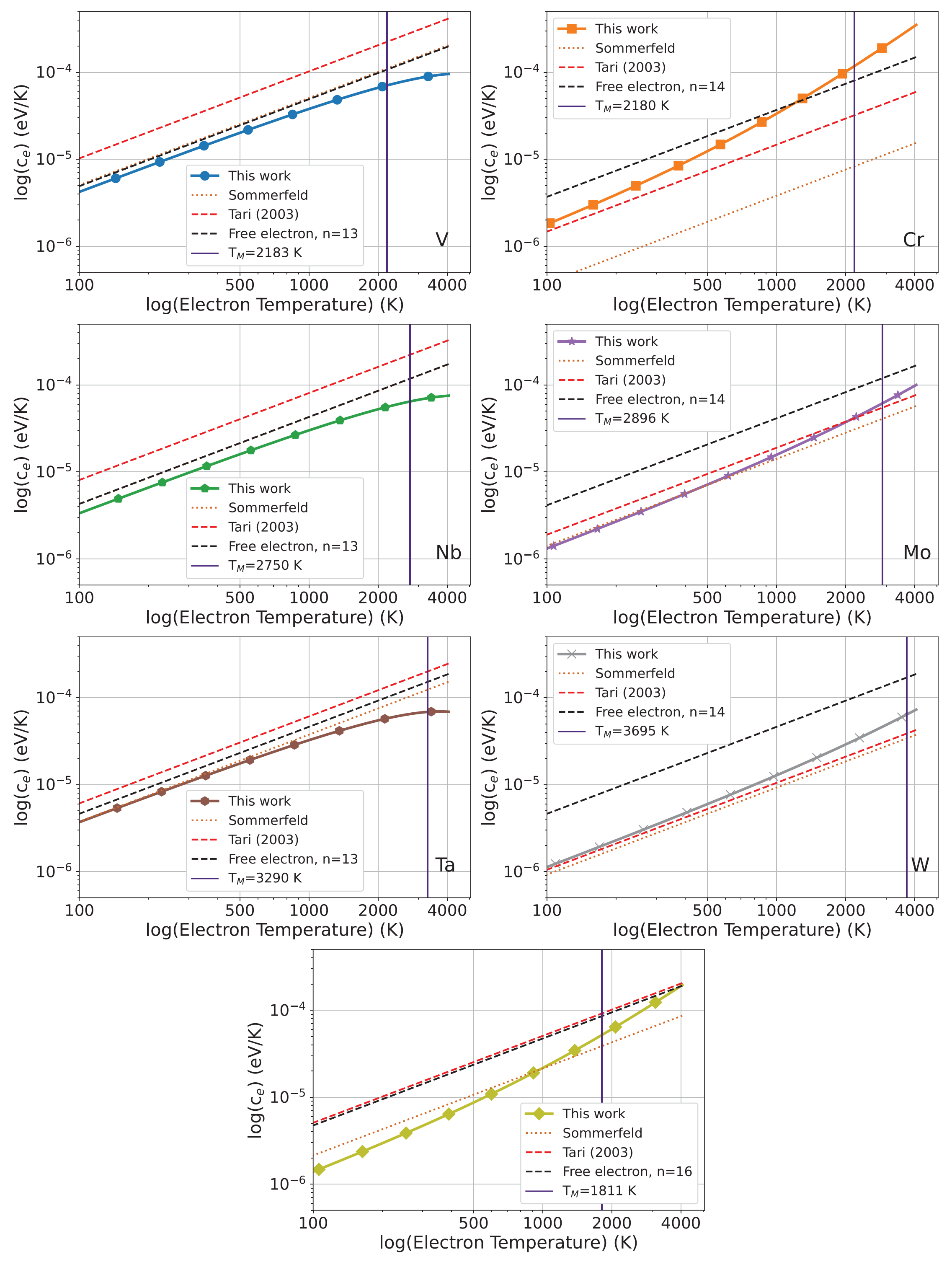

Figure 2. Electronic heat capacity in a primitive cell as a function of temperature from finite temperature differences. The black dashed lines are the free electron model values, n indicates the number of electrons used. The dotted lines are the Sommerfeld approximations. The red lines are the heat capacity from low-temperature experiments from [37] that were extrapolated at higher temperatures using $C_e = \gamma T$.

3. Electron-impurity scattering times

3.1. Background

To calculate the scattering time of electron-impurity, the assumptions made by Ashcroft and Mermin [1] were used;

(i) Scattering only occurs in a band n with a wave vector k to a band n' with a wave vector k', where $n = n'$.

(ii) Electron spin is conserved during the scattering.

(iii) Scattering can only happen in states that are unoccupied (due to Pauli's exclusion principle).

From these assumptions, the scattering probability at a time τ at k for all k' is defined as [1],

$$\frac{1}{\tau(k)} = \int \frac{\mathrm{d}k'}{(2\pi)^3} W_{k,k'}\left[1 - g(k')\right] \tag{13}$$

where $W_{k,k'}$ is the probability of an electron scattering from k to k', and $g(k')$ is the density of states at k'.

The scattering probability, is related to the transition probability of an electron [1],

$$W_{k,k'} = \frac{2\pi}{\hbar} n_i \delta\left(\epsilon(k) - \epsilon(k')\right) \left|\langle k'|\,U|k\rangle\right|^2 \tag{14}$$

where n_i is the number of defects per volume, $\delta(\epsilon(k) - \epsilon(k'))$ is the density of states at Fermi energy $g(\epsilon_\mathrm{F})$, and $\langle k'|\,U|k\rangle$ is the Fermi's Golden rule for the transition probability of an electron with a potential energy of U (also known as perturbation potential) from k to k'. The Fermi's golden rule can be solved as,

$$\langle k'|\,U|k\rangle = \int \mathrm{d}r \psi_k^*(r)\,U(r)\,\psi_k(r) \tag{15}$$

Further, assuming that the potential is uniform across the system, $U(r) \to U$, equation (15) becomes,

$$\langle k'|\,U|k\rangle = U \int \mathrm{d}r \psi_k^*(r)\,\psi_k(r) = U \times v_\mathrm{cell} \tag{16}$$

where v_cell is the volume of the supercell. Hence, $W_{k,k'}$ becomes,

$$W_{k,k'} = \frac{2\pi}{\hbar} n_{ig}(\epsilon_\mathrm{F})\,(U \times v_\mathrm{cell})^2 \tag{17}$$

Finally, the scattering probability equation reduces to,

$$\frac{1}{\tau(k)} = \frac{2\pi}{\hbar} n_i g(\epsilon_\mathrm{F})\,(U \times v_\mathrm{cell})^2 \int \frac{\mathrm{d}}{k}(2\pi)^3 \tag{18}$$

with $\int \mathrm{d}k' = (2\pi)^3 / v_\mathrm{cell}$,

$$\frac{1}{\tau} = \frac{2\pi}{\hbar} n_i g(\epsilon_\mathrm{F})\,v_\mathrm{cell} U^2 \tag{19}$$

VASP can output the local potential (V_LOCPOT) from DFT calculations as,

$$V_\mathrm{LOCPOT}(r) = V_\mathrm{ionic}(r) + V_\mathrm{H}(r) + V_\mathrm{XC}(r) \tag{20}$$

Where, $V_\mathrm{ionic}(r)$ is the ionic contribution to the potential, $V_\mathrm{H}(r)$ is the Hartree potential, and $V_\mathrm{XC}(r)$ is the potential from the exchange-correlation potential.

To validate the scattering probability equation, the electric resistivity of FP were calculated. The resistivity is defined as [1],

$$\rho = \frac{m_\mathrm{e}}{ne^2\tau} \tag{21}$$

where m_e is the electron mass 9.109×10^{-31} kg, n is the electron density of states per atom, $n = \frac{1}{v_\mathrm{cell}} \int_{-\infty}^{\epsilon_\mathrm{F}} g(\epsilon)\mathrm{d}\epsilon$, τ is the scattering time.
Mason [2] showed that the total scattering time can be calculated as,

$$\tau = \tau_\mathrm{nn} + \left(\frac{1}{\tau_\mathrm{imp}} + \frac{1}{\tau_\mathrm{e-ph}} + \frac{1}{\tau_\mathrm{e-e}}\right)^{-1} \tag{22}$$

where τ_nn, τ_imp, $\tau_\mathrm{e-ph}$, and $\tau_\mathrm{e-e}$ are respectively the scattering time that arises for the smallest scattering distance, electron-impurities, electron–phonon, and electron–electron scattering. The shortest distance is defined by the nearest-neighbour distance, which for BCC transition metals is $a\sqrt{3/4}$ where a is the lattice parameter, and the speed at which the electrons travel in the conduction band is the defined by the Fermi velocity. Thus, the smallest scattering probability allowed is,

$$\tau_{\mathrm{nn}} = \frac{a\sqrt{3/4}}{v_f}. \tag{23}$$

The τ_{nn} and $1/\tau_{\mathrm{imp}}$ are taken to be temperature-independent, whereas $1/\tau_{\mathrm{e-ph}}$ is proportional to T^3 at $T < \Theta_{\mathrm{D}}$, where Θ_{D} is the Debye temperature, and T at $T \geqslant \Theta_{\mathrm{D}}$. And $1/\tau_{\mathrm{e-e}}$ is proportional to T^2 [2]. Due to the high defect concentration in the structures with the defects (1 defect for every 250 atoms), the contributions are approximated up to the first temperature approximation; hence the $1/\tau_{\mathrm{e-e}}$ contribution will be ignored as it scales with T^2. In a model with a lower defect concentration, the e–e contribution should be included to improve the accuracy of the model. Using the Matthiessen's rule the total resistivity is then,

$$\rho = \rho_{\mathrm{nn}} + \rho_{\mathrm{imp}} + \rho_{\mathrm{e-ph}}\left(T\right) \tag{24}$$

where ρ_{nn}, ρ_{imp}, and $\rho_{\mathrm{e-ph}}(T)$, are respectively the resistivities that arise from the shortest distance, electron-impurities, and electron–phonon scattering. The various components will be analysed in the following sections. In this section, the focus will be on the electron-impurities, which is related to the FP resistivity. The electron-impurities can be further split down to individual components, i.e. the resistivity that would arise from electron scattering on vacancies, dumbbells, crowdions, and other defects. The Matthiessen's rule [1] can also be used to subdivide the Frenkel Pair resistivity using the vacancy and interstitial scattering time as,

$$\rho_{\mathrm{FP}} = \frac{m_{\mathrm{e}}}{ne^2\tau_{\mathrm{vac}}} + \frac{m_{\mathrm{e}}}{ne^2\tau_{\mathrm{int}}} \tag{25}$$

and τ_{vac} and τ_{int} are respectively the scattering time for an electron-vacancy and electron-interstitial interaction.
While to calculate the electronic thermal conductivity [1],

$$\kappa_{\mathrm{e}} = \frac{1}{3}c_{\mathrm{e}}v_{\mathrm{F}}^2\tau_{\mathrm{e}} \tag{26}$$

similarly to the resistivity, one can apply the Matthiessen's rule and using equation (22) to find individual components of the electron thermal conductivity, i.e.

$$\kappa_{\mathrm{e}} = \kappa_{\mathrm{nn}} + \left(\frac{1}{\kappa_{\mathrm{imp}}} + \frac{1}{\kappa_{\mathrm{e-ph}}}\right)^{-1} \tag{27}$$

and specifically for the case of electron-impurities,

$$\kappa_{\mathrm{imp}} = \left(\frac{1}{\kappa_{\mathrm{vac}}} + \frac{1}{\kappa_{\mathrm{int}}}\right)^{-1}. \tag{28}$$

The potentials were extracted from the different cells using PyVista [38]. A 3D model was created using the LOCPOT file generated by VASP. Then, PyVista slicing function was used to create 1028 planes by slicing in the x, y, z directions and 2048 planes were used by slicing in the [111] directions. The slicing in the [111] direction was not done for the full length, but in the range of $\frac{a}{2}[111] \leqslant x \leqslant \frac{9a}{2}[111]$, this is to avoid artefacts at the edges of the cell. For Fe, the [110] direction was used, due to the [110] dumbbell. Then the potential values in each plane were averaged to obtain an average point value that could be then plotted. The potential difference was calculated for each defect. For the vacancy, the potential value was taken to be the potential minima and averaged across all four directions and then divided by two. For Fe and Cr, which included the magnetic moments, the potential is split in up and down components. The potentials were treated separately, and averaged at the end. For the dumbbell, and crowdion defect, this was taken to be the difference between the maxima and the minima in the direction of the defect divided by two. The dumbbell and crowdion potentials were taken in the region enclosed by the nearest-neighbours of the defect, with the following method,

(i) Find the region enclosed by the nearest neighbours of the defect in the defect direction. Nearest neighbour in BCC transition metal is $\sqrt{3}/2 \times a$, where a is the lattice parameter.

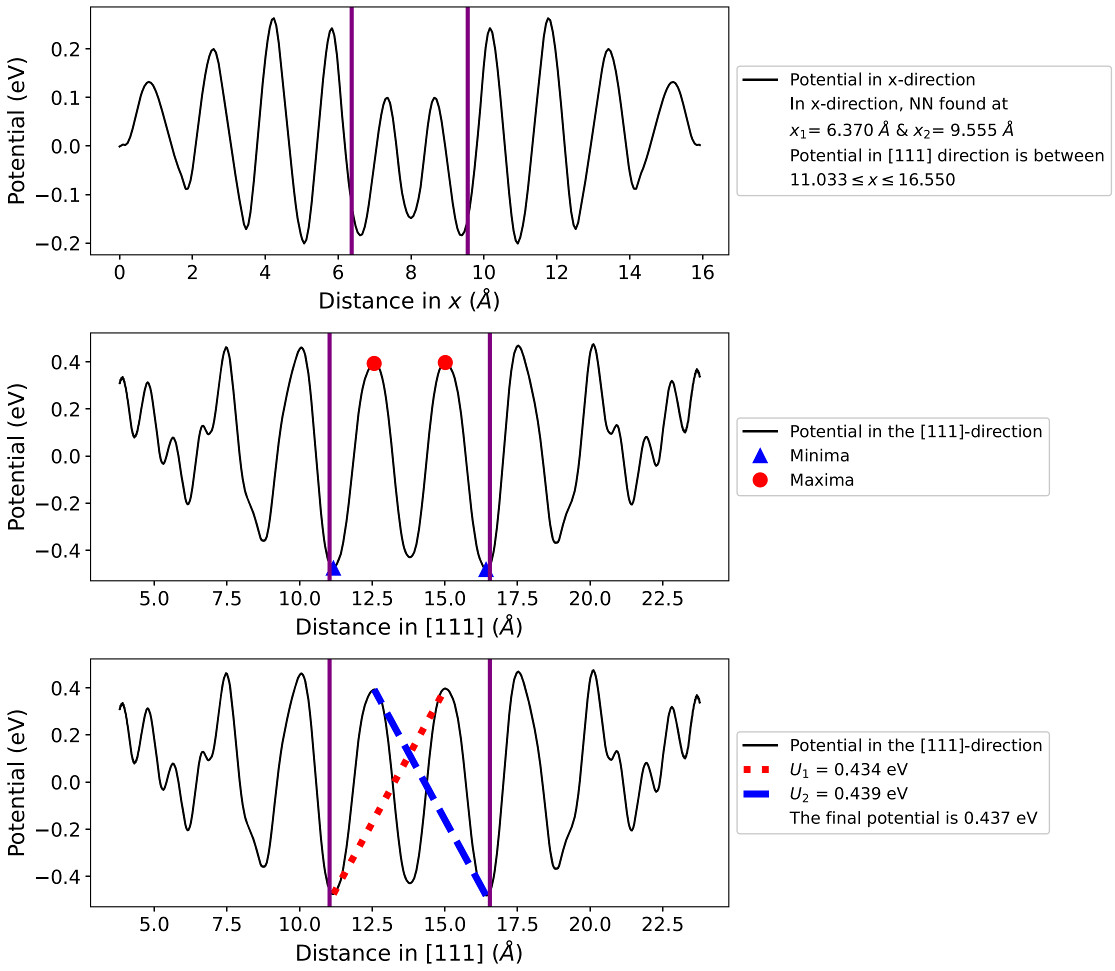

Figure 3. Potential value extraction from the perturbation potential between the perfect and [111] dumbbell supercells in W.

(ii) Find the maxima and minima in the defect direction.

(iii) Then the final potential value is given by $(\bar{U}_{\text{max}} - \bar{U}_{\text{min}})/2$, and averaged across as many combinations of U_{min} and U_{max} there are.

Each potential was unique for each defect and element. The process is shown in figure 3 for the [111] dumbbell in W, further explanation behind these choices is discussed in appendix.

3.2. Results

The defect formation energies were calculated using equation (1), and they were compared with available literature data. These results are shown in table 4. The formation energies match with the literature data and experimental data (where available). There is no strong difference between crowdion and dumbbell defects in the [111] direction. In figure 4, the density of states of the various elements is shown for the pure, mono-vacancy, dumbbell, and crowdion structures. The graph shows the values per eV atom^{-1}, however, in the equations the total value of $g(\epsilon_F)$ were used. Chromium has a very small density of states at Fermi energy, and this matches with the primitive cell calculations.

The perturbation potentials values for the Frenkel defects have been reported in appendix in table A1. To validate the potentials value, the resistivities of BCC transition metals defects were calculated and compared with available experimental data, these results have been compiled in table 5. It is noted that the experimental vacancy resistivity values in table 5 are that the resistivity values were measured using differential thermal analysis (DTA), and electrical resistivity measurements (ERM) which can have errors up to one order of magnitude [42]. To reduce these errors the samples are quenched to room temperature, which would maintain the number of vacancies caused by the irradiation, and reduce the errors of ERM and DTA measurements. However, quenching a sample can generate additional vacancies due to strain [43], and these can alter the final result of the resistivity measurements. However, this work correctly predicts the vacancy resistivity of W, and this is because the measurements for W were

Table 4. Comparison of the Frenkel pair formation energies. H_f^{vac} is the formation energy of a mono-vacancy, H_f^{db} is the formation energy of a dumbbell defect, H_f^{cd} formation energy of a crowdion.

Element	V	Nb	Ta	Cr	Mo	W	Fe
H_f^{vac}	2.484^{a} 2.51^{b} 2.1^{d}	2.686^{a} 2.99^{b} 2.7^{d}	2.961^{a} 3.14^{b} 3.1^{d}	2.655^{a} 2.64^{b} 2.1^{d}	2.820^{a} 2.96^{b} 3.1^{d}	3.163^{a} 3.56^{b} 3.6^{d}	2.339^{a} 2.15^{c} $1.8\text{-}2.0^{d}$
H_f^{db}	2.853^{a} 3.367^{b}	3.913^{a} 5.253^{b}	4.811^{a} 5.832^{b}	6.458^{a} 5.685^{b}	7.677^{a} 7.417^{b}	10.379^{a} 9.548^{b}	4.682^{a*} 3.93^{c}
H_f^{cd}	2.853^{a} 3.371^{b}	3.913^{a} 5.254^{b}	4.811^{a} 5.836^{b}	6.415 5.660^{b}	7.677^{a} 7.419^{b}	10.380^{a} 9.551^{b}	/

[a] This work

[a*] [110] dumbbell.

[b] First principles, Nguyen-Manh, Horsfield, Dudarev [39].

[c] First principles, Derlet, Nguyen-Manh, Dudarev [40].

[d] Experimental from Schultz [41].

by comparing and fitting field ion microscopy and ERM for the 7 $\mu\Omega$m value, and transmission electron microscopy combined with ERM for 6.3 $\mu\Omega$m [42, 43]. For the reference values for the resistivities of Frenkel Pair in table 5, Broeders and Konobeyev collected various experimental and analytical data, from x-ray diffraction methods, electron irradiation at low temperature of single crystals, experiments with polycrystals, analysis of various experiments and data obtained by fitting resistivities equations [44]. By statistical analysis and the relative accuracy of the methods, they evaluated the values used in their work [44].

From the results, the crowdion resistivities are lower than the dumbbell ones. The majority of this difference comes from the extraction method of the perturbation potential. Dumbbells and crowdions are topologically different, the dumbbell is a 0-dimensional defect, while the crowdion is a 1-dimension defect. Hence, the method developed for dumbbells is not feasible to be used for the crowdions. The crowdions will require a treatment that considers the [111] crowdion influence on the whole [111] string, like the Frenkel–Kontorova model used by Fitzgerald and Nguyen-Manh [30]. Furthermore, this suggests that in dislocations, the electron-dislocation scattering time will be positionally dependent. This is outside the scope of this work, and it will now focus on the 0-dimensional defects like vacancies and dumbbells. Due to the high-concentration of defects, 1 per every 250 atoms, the electronic thermal conductivity is local to the defect and cannot be compared to the bulk thermal conductivity directly as shown in table 6. This leads to the large discrepancy between the calculated values and the experimental ones from Ho, Powell, and Lily [45]. The results were also compared with the nearest-neighbour limit thermal conductivity calculated from the values reported by Mason [2]. While they are on the same order of magnitude, the values of the electron-impurities from Mason differ from the one calculated in this work due to many reasons; Mason used experimental lattice parameters, their Fermi velocity is different, and the heat capacity also slightly differs. These lead to the differences in the values. Group VI transition metals and Fe are the closest, while in group V these are higher than the values from Mason. In the FP case, the smallest value dominates the thermal conductivity due to the application of the Matthiessen's rule. The vacancy and the dumbbell defects have lower thermal conductivity when compared to the crowdion, which is the opposite effect seen in the resistivity.

4. Electron–phonon scattering times and correction factors

4.1. Electron–phonon contribution

Mason in their work [2] used the Kaganov model to approximate the electron–phonon scattering time. Assuming that the electron temperature is the same as the lattice temperature, T_l, the Kaganov model is defined as [46],

$$\left.\frac{\partial E}{\partial t}\right|_{\mathrm{e-ph}} = GT_\mathrm{l} \quad G = \frac{\pi^2 m^* v_\mathrm{s}^2 N_\mathrm{e}}{6\tau_{\mathrm{e-ph}} T_\mathrm{l}} \tag{29}$$

where G is the phonon coupling strength, v_s is the speed of sound in the material, $\tau_{\mathrm{e-ph}}$ is the electron–phonon scattering time, m^* is the effective mass, and N_e is the number of electrons, $N_\mathrm{e} = \int_{-\infty}^{\epsilon_\mathrm{F}} g(\epsilon)\mathrm{d}\epsilon$.

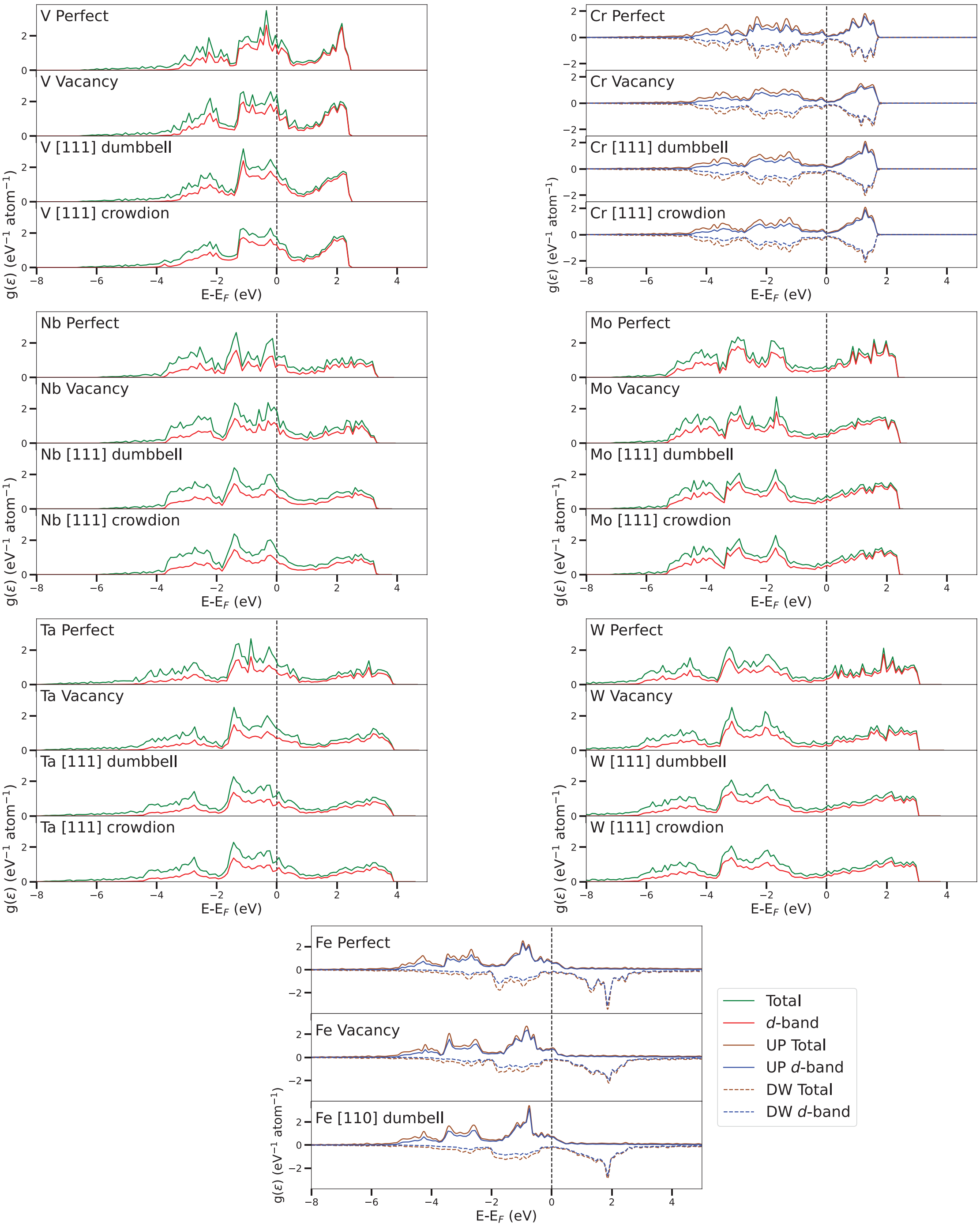

Figure 4. Supercell density of states of BCC transition metals centred at Fermi energy, with tetrahedron smearing and a 0.1 eV energy step. Fe and Cr included magnetic moments in the simulations, hence the difference in DOS up and DOS down. The presence of defects affects the DOS. The contribution from *d*-electrons is also shown.

To find the electron–phonon coupling strength, the temperature dependent derivation by Lin [47] is used,

$$G(T_1) = \frac{\pi \hbar k_B \lambda \langle \omega^2 \rangle}{g(\epsilon_F)} \int_{-\infty}^{\infty} g(\epsilon)^2 \left(-\frac{\partial f}{\partial \epsilon} \right) d\epsilon \tag{30}$$

where the $\frac{\partial f}{\partial \epsilon}$ is the derivative of the Fermi–Dirac function in respect of energy, λ is the first reciprocal moment of the Eliashberg spectral function, and $\langle \omega^2 \rangle$ is the second moment of the phonon density of states. This results in,

Table 5. Comparison of Frenkel pairs resistivities in BCC transition metals.

	This work ($\mu\Omega$m)					References ($\mu\Omega$m)	
Element	ρ_{vac}	ρ_{db}	ρ_{cd}	$\rho_{\mathrm{vac-db}}$	$\rho_{\mathrm{vac-cd}}$	ρ_{vac} [42]	ρ_{FP} [44]
V	22.2	11.6	7.0	33.9	29.2		21
Nb	31.0	17.4	7.0	48.4	38.0		14
Ta	20.0	19.8	2.9	39.8	22.8	8.5	16.5
Cr[6]	6.0	7.7	0.6	13.7	6.6		37
Mo	9.2	16.8	1.1	26.0	10.3	4.3	13.4
W	7.9	10.7	0.6	18.6	8.5	6.3[8] / 7[4,5]	27
Fe[7]	20.1	31.1	/	51.1	/		24.6

[6] Spin polarized anti-ferromagnetic.

[7] Spin polarized ferromagnetic, [110] dumbbell.

[8] Field Ion Microscopy and resistivity measurements [42]

[9] Comparison of Differential Dilatometry and quenching resistivity [42].

[10] Transmission electron microscopy and resistivity [42].

Table 6. Comparison of Frenkel pairs electron thermal conductivities in BCC transition metals at 300 K.

	This work (W mK)$^{-1}$						References (W mK)$^{-1}$	
Element	κ_{nn}	κ_{vac}	κ_{db}	κ_{cd}	$\kappa_{\mathrm{vac-db}}$	$\kappa_{\mathrm{vac-cd}}$	κ_{nn}* [2]	Exper. [45]
V	6.89	0.024	0.045	0.075	0.016	0.018	3.70	30.7
Nb	5.35	0.019	0.034	0.084	0.012	0.016	3.74	53.7
Ta	5.82	0.032	0.033	0.225	0.016	0.028	3.28	57.5
Cr[11]	2.18	0.026	0.020	0.241	0.011	0.023	1.99	93.7
Mo	2.83	0.034	0.018	0.289	0.012	0.030	2.23	138
W	2.37	0.034	0.025	0.427	0.014	0.031	1.42	174
Fe[12]	2.93	0.008	0.005	/	0.003	/	2.57	80.2

* Calculated using values reported in [2].

[11] Spin polarized anti-ferromagnetic.

[12] Spin polarized ferromagnetic, [110] dumbbell.

Table 7. Parameters needed to define the electron–phonon contribution, and the Debye temperature.

Element	$\lambda\langle\omega^2\rangle$ meV^{-2}	v_s (m s)$^{-1}$ [48]	Θ_D (K) at 298 K [45]
V	281.6[a]	4560	390
Nb	275[b]	3480	260
Ta	165.44[c]	3400	225
Cr[1]	128.31[a]	5940	424
Mo	118.8[d]	6190	377
W	110.5[a]	5174	312
Fe[2]	738[e]	4910	373

[1] Spin polarized anti-ferromagnetic.

[2] Spin polarized magnetic moments included.

The values for $\lambda\langle\omega^2\rangle$ are from [a]-[49], [b]-[50], [c]-[51], [d]-[52], and [e]-[53].

$$\frac{1}{\tau_{\mathrm{e-ph}}}(T_1) = \frac{6GT_1}{\pi^2 m^* v_s^2 N_e} \tag{31}$$

The values of $\lambda\langle\omega^2\rangle$ were collated by Mason [2] and are shown in table 7, which also has the speed of sound, and the Debye temperatures (Θ_D), the effective mass values are absolute values from table 3.

To validate the electron–phonon scattering time the tungsten results were compared with the values reported by Hofmann *et al* [8] in their supplementary information, where they fitted the thermal diffusivity data to obtain the scattering time for the electron-impurity, electron–phonon and electron–electron scatterings. Specifically, the electron–phonon scatterings are compared, and shown in figure 5. The electron–phonon from the perfect cell is slightly higher than the results from Hofmann *et al* [8]. There are a few reasons for these differences, in the current model, the speed of sound and the effective

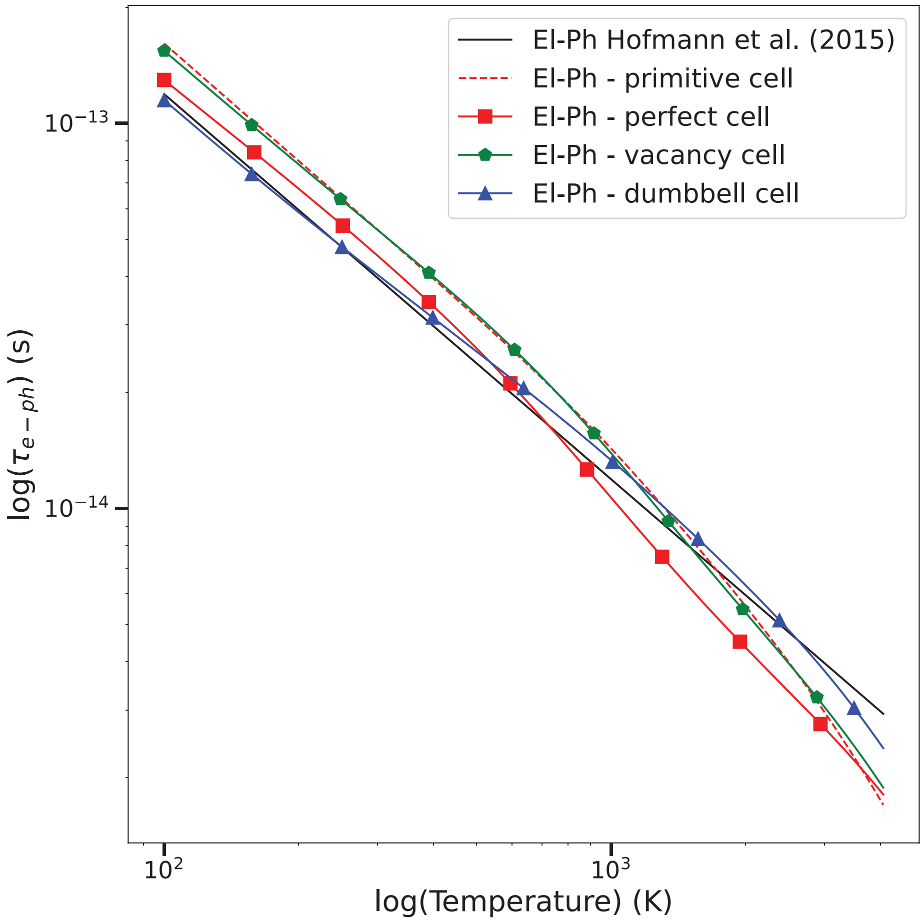

Figure 5. Comparison of electron–phonon (El-Ph) scattering rates for the supercell structures; perfect, vacancy, and [111] dumbbell structures in W from Kaganov model, and W primitive cell. And, comparison with experimental fitting done by Hofmann *et al* [8].

mass are fixed values rather than dependent on temperature, and the changes in the Debye temperature are not accounted either. Furthermore, Hofmann *et al* pure W values were experimentally measured up to 473 K [8], hence extending their fitted value beyond 473 K might lose on high-temperature changes. However, it is an acceptable difference, as it should provide a good estimate of the trend. The perfect electron–phonon scattering time from the primitive cell is similar to the supercells' vacancy, and larger than the dumbbell electron–phonon times at lower temperatures, but they all converge towards the perfect electron–phonon scattering time at higher temperatures. While the perfect supercell electron–phonon time sits between the vacancy and dumbbell scattering time at lower temperatures, while converging to the primitive perfect electron–phonon at higher temperatures. This indicates that at higher temperatures, the electron–phonon scattering probability is in the same order of magnitude.

4.2. Temperature dependent correction factors for resistivity from Mott model

The scattering time derived is temperature-independent, and this is because the scattering rate of electrons to an impurity does not change with temperature. But what does change with temperature is the scattering from the *s*-band to the *d*-band [23, 54]. Electron–electron scatterings are assumed to be an intra-process, i.e. *s*-electrons will only collide with other *s*-electrons and will not have enough energy to escape the *s*-energy level. However, *s*-electron and phonons collision can lead the *s*-electron to scatter in another *s*-state or in a *d*-state [54]. In *d*-block transition metals, the *d*-band is not fully occupied, which means that it has some 'holes' available for other electrons to take. However, when a phonon collides with an *s*-electron, the additional vibrational energy, enables *s*-electrons to jump to the empty states of the *d*-band [54]. This is limited to electrons that match the spin of the hole, to maintain the Pauli's exclusion principle; if the space is occupied by a spin up electron, then the *s*-electron must have spin down to scatter to this state.

Therefore, a correction factor needs to be included to account for the scattering from *s*-band to the *d*-band in the electron–phonon resistivity and thermal conductivity. For non-magnetic transition metals, the resistivity equation with the correction factor should be applied to the electron–phonon scattering time as [54–56],

$$\rho_{\mathrm{e-ph}}(T) = \frac{m_{\mathrm{e}}}{ne^{2}\tau_{\mathrm{e-ph}}(T)}\left[1 - A_{\rho}T_{\mathrm{l}}^{2}\right] \tag{32}$$

According to Mott [54], A_{ρ} is defined as,

$$A_{\rho} = \frac{(\pi k_{\mathrm{B}})^{2}}{6}\left[3\left(\frac{\tau'}{\tau}\right)^{2} - \frac{\tau''}{\tau}\right], \tag{33}$$

where τ', and τ'' are derivatives of the scattering time as a function of energy. Since the scattering time is dependent on the density of states at Fermi energy, $g(\epsilon_{\mathrm{F}})$, and the conduction electron transition probability is dependent on the available holes in the *d*-band, the temperature degeneracy is therefore dependent on the slope and the curvature of the density of states at Fermi energy of the *d*-band. As shown by Aisaka and Shimizu [55] and Chiu [56] the correction factor is,

$$A_{\rho} = \frac{(\pi k_{\mathrm{B}})^{2}}{6}\left[3\left(\frac{g_{d}(\epsilon)'}{g_{d}(\epsilon)}\right)^{2} - \frac{g_{d}(\epsilon)''}{g_{d}(\epsilon)}\right]_{\epsilon_{\mathrm{F}}} \tag{34}$$

Finally, by substituting for *A*,

$$\rho_{\mathrm{e-ph}}(T) = \frac{m_{\mathrm{e}}}{ne^{2}\tau_{\mathrm{e-ph}}(T)}\left(1 - \frac{(\pi k_{\mathrm{B}}T_{\mathrm{l}})^{2}}{6}\left[3\left(\frac{g_{d}(\epsilon)'}{g_{d}(\epsilon)}\right)^{2} - \frac{g_{d}(\epsilon)''}{g_{d}(\epsilon)}\right]_{\epsilon_{\mathrm{F}}}\right). \tag{35}$$

For magnetic materials, the holes in the d-band will have a magnetic spin equal and opposite to that of the magnetic field, while an occupied state will have the magnetic spin parallel to that of the magnetic field [57]. Which means that the electron not only has to match the electron spin, but also the magnetic spin of the hole. Thus, reducing the probability of a collision to result in a jump from *s* to *d*-band. And as the probability of the jump is reduced, the electron resistivity should increase by a maximum factor of 2 [57]. Mott and Wills [54] proved that the resistivity caused by impurities should increase by a factor of $2^{2/3}$ up to the Curie temperature (T_{C}). And, above the Curie temperature, the resistivity will be dependent on A_{ρ} [54] as shown in equation (32). The changes at the Curie temperature are because below the Curie temperatures *s*-electrons will have to match the spin direction available in the *d*-shell holes and be antiparallel to the magnetic field. While, above the Curie temperature, there is no magnetic field, and there will be more holes with more spin directions available, hence allowing the conduction electrons to scatter in the *d*-shell [54]. From this, it can be deduced that below Curie temperature (T_{C}),

$$\rho_{\mathrm{e-ph}}(T) = \frac{m_{\mathrm{e}}}{ne^{2}\tau_{\mathrm{e-ph}}(T)}\left(1 + \left(2^{2/3} - 1\right)\frac{T_{\mathrm{l}}}{T_{\mathrm{C}}}\right) \tag{36}$$

Above the Curie temperature, the resistivity will have the same form as the paramagnetic metals, shown in equation (35). Finally, the temperature dependent impurity scattering probability for magnetic metals is given by,

$$\rho_{\mathrm{e-ph}}(T) = \begin{cases} \frac{m_{\mathrm{e}}}{ne^{2}\tau_{\mathrm{e-ph}}(T)}\left(1 + \left(2^{2/3} - 1\right)\frac{T_{\mathrm{l}}}{T_{\mathrm{C}}}\right) & \text{for } T_{\mathrm{l}} \leqslant T_{\mathrm{C}} \\ \frac{m_{\mathrm{e}}}{ne^{2}\tau_{\mathrm{e-ph}}(T)}\left(1 - \frac{(\pi k_{\mathrm{B}}T_{\mathrm{l}})^{2}}{6}\left[3\left(\frac{g_{d}(\epsilon)'}{g_{d}(\epsilon)}\right)^{2} - \frac{g_{d}(\epsilon)''}{g_{d}(\epsilon)}\right]_{\epsilon_{\mathrm{F}}}\right) & \text{for } T_{\mathrm{l}} > T_{\mathrm{C}} \end{cases} \tag{37}$$

using these equations, a temperature dependent scattering can be calculated, as well as temperature dependent impurity resistivity.

The Mott correction for the *s*-*d* scatterings arise from the scattering of the conduction electrons due to the presence of phonons [54]. Therefore, changes in the electron's scattering rate will not only affect the resistivity, but also the thermal conductivity. Hence, if a correction factor is applied to the resistivity, this should also be applied to the thermal conductivity. Following the Mott model [54], the thermal conductivity correction factor should help increase the electron thermal conductivity, as such the e–ph correction thermal conductivity for non-ferromagnetic is,

$$\kappa_{\mathrm{e-ph}}(T) = \frac{1}{3}c_{\mathrm{e}}v_{\mathrm{F}}^{2}\tau_{\mathrm{e-ph}}(T)\left[1 + A_{\kappa}T_{\mathrm{l}}^{2}\right], \tag{38}$$

Table 8. Density of states and its derivatives at Fermi energy of the *d*-band for tetrahedron with Blöch corrections smearing and $\Delta E = 0.1$ eV.

	Perfect			Vacancy			Dumbbell		
Element	$g_d(\epsilon)$	$g_d'(\epsilon)$	$g_d''(\epsilon)$	$g_d(\epsilon)$	$g_d'(\epsilon)$	$g_d''(\epsilon)$	$g_d(\epsilon)$	$g_d'(\epsilon)$	$g_d''(\epsilon)$
V	308	−376	−576	421	−646	−3353	343	−544	45
Nb	143	−236	5384	270	−825	−2193	197	−434	1029
Ta	182	−437	622	169	−165	734	180	271	−460
Cr[1]	42	−621	4397	41	−337	3214	66	−396	1927
Mo	102	−42	512	88	160	1394	143	49	−1075
W	79	158	577	75	−17	−218	93	124	−889
Fe[2]	192	−435	530	223	−60	−3177	210	−270	−1163

The units of $g_d(\epsilon)$, $g_d'(\epsilon)$, and $g_d''(\epsilon)$ are respectively eV^{-1}, eV^{-2}, and eV^{-3}

[1] Spin polarized anti-ferromagnetic.

[2] Spin polarized ferromagnetic, [110] dumbbell.

and A_κ is given by Aisaka and Shimizu as [55],

$$A_\kappa = \frac{(\pi k_\mathrm{B})^2}{6}\left[\frac{37}{5}\left(\frac{g_d(\epsilon)'}{g_d(\epsilon)}\right)^2 - \frac{21}{5}\frac{g_d(\epsilon)''}{g_d(\epsilon)}\right]_{\epsilon_\mathrm{F}} \tag{39}$$

therefore, the correction factor for non-ferromagnetic is,

$$\kappa_{\mathrm{e-ph}}(T) = \frac{1}{3}c_\mathrm{e}v_\mathrm{F}^2\tau_{\mathrm{e-ph}}(T)\left[1 + \frac{(\pi k_\mathrm{B}T_\mathrm{l})^2}{6}\left[\frac{37}{5}\left(\frac{g_d(\epsilon)'}{g_d(\epsilon)}\right)^2 - \frac{21}{5}\frac{g_d(\epsilon)''}{g_d(\epsilon)}\right]_{\epsilon_\mathrm{F}}\right]. \tag{40}$$

And for ferromagnetic materials this is,

$$\kappa_{\mathrm{e-ph}}(T) = \begin{cases} \frac{1}{3}c_\mathrm{e}v_\mathrm{F}^2\tau_{\mathrm{e-ph}}(T)\left(1-\left(2^{2/3}-1\right)\frac{T_\mathrm{l}}{T_\mathrm{C}}\right) & \text{for } T_\mathrm{l} \leqslant T_\mathrm{C} \\ \frac{1}{3}c_\mathrm{e}v_\mathrm{F}^2\tau_{\mathrm{e-ph}}(T)\left(1 + \frac{(\pi k_\mathrm{B}T_\mathrm{l})^2}{6}\left[\frac{37}{5}\left(\frac{g_d(\epsilon)'}{g_d(\epsilon)}\right)^2 - \frac{21}{5}\frac{g_d(\epsilon)''}{g_d(\epsilon)}\right]_{\epsilon_\mathrm{F}}\right) & \text{for } T_\mathrm{l} > T_\mathrm{C} \end{cases}. \tag{41}$$

In the simulations, the density of states was fitted with a cubic spline using SciPy [58] and then the gradient was found using NumPy gradient [34]. From these, the values of the *d*-band density of states and its derivatives were extracted.

Table 8 shows the values of the *d*-band density of states and its derivatives at Fermi energy. One surprising feature is that in group VI, the vacancy have a lower density of states value than the perfect cell, indicating that is a more stable structure. Furthermore, figure 6 shows the comparison of the electron–phonon correction factor for the resistivity, between the primitive and perfect supercell on the left and the supercell with defects on the right. They had the same smearing, tetrahedron with Blöch corrections, with an energy mesh of $\Delta E = 0.1$ eV. As it can be deduced by the graphs, the Mott correction factor is strongly affected by the number of atoms. This arises from equation (34), where small changes of the DOS at Fermi energy will entirely change the correction factor, leading to each Frenkel defect having different behaviours. The number of atoms will affect the DOS value at Fermi energy, thus changing the correction factor.

Figure 7 shows the ratio of the resistivity and the resistivity at 300 K of Frenkel defects in BCC transition metals. The ratio between the resistivities and the resistivity at 300 K follows the same pattern as shown in figure 6(b). Overall, the resistivity decreases when the Mott correction factors are included. In some cases, the resistivity first increases, but then it starts to decrease. Cr and Nb have the largest impact from the correction factors. In Fe, the change in the ratio of the resistivities due to the Curie temperature is evident. In Ta and Mo, the vacancy causes an increase in the resistivity.

Figure 8 shows the thermal total thermal conductivity of the Frenkel defects in BCC transition metals. The κ_e is in log function to showcase the small changes in the thermal conductivity. The perfect electron–phonon thermal conductivity is higher than experimental one in most cases, except for Nb, where is smaller. Introducing the nearest neighbour limit takes away differences from the defects. The thermal conductivity will keep increasing until it matches with the combined electron–phonon with nearest neighbour limit, as from the Matthiessen's rule the smallest contributor dominates the thermal conductivity. This can be seen in both Fe and Nb. The Frenkel defect thermal conductivity approaches

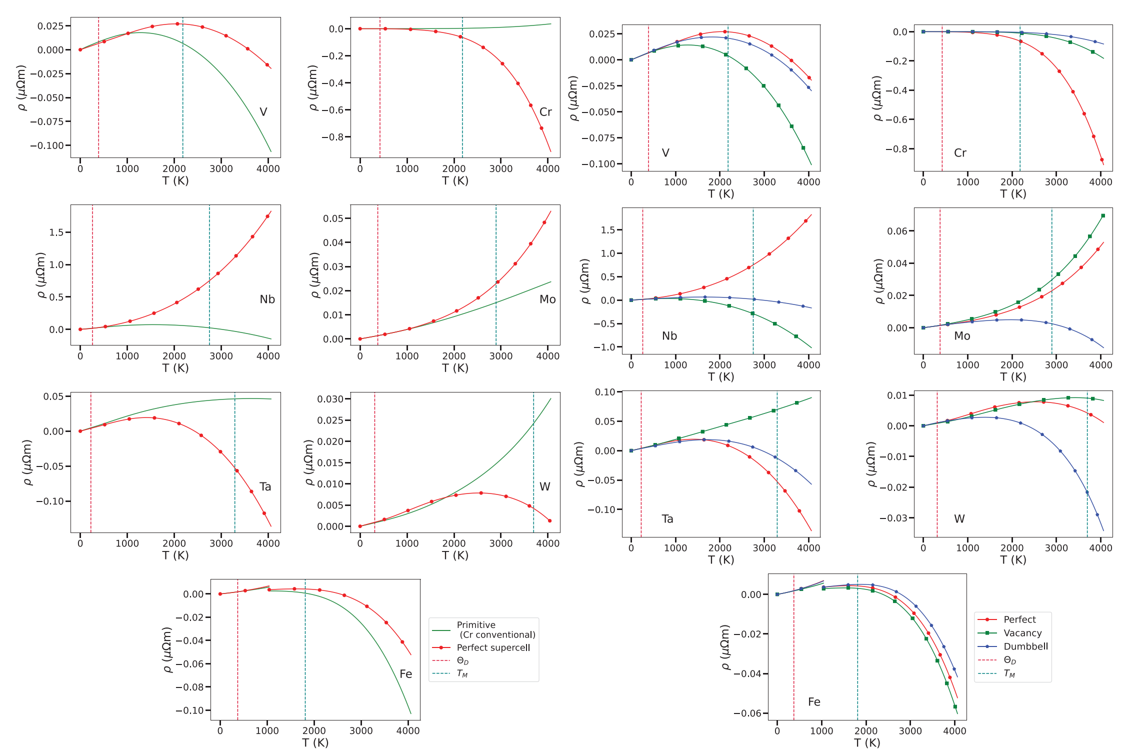

(a) Comparison of primitive cell tetrahedron with Blöch corrections (Cr is a conventional cell) and perfect supercell result.

(b) Tetrahedron with Blöch corrections.

Figure 6. Comparison of the effect of density of states on the electron–phonon correction factor in BCC transition metals. All DOS have a $\Delta E = 0.1$ eV.

the experimental thermal conductivity close to the melting points of the material. The electron–phonon contribution for Fe and Cr is larger than the other BCC transition metals, this might suggest that the electron–phonon scattering requires a correction to account for the magnetic moments.

5. Realistic FP concentrations

The model would be imperfect if it could not predict resistivity and electron thermal conductivity for realistic Frenkel defect concentrations. As the scattering time is measured over a single defect, the realistic scattering time can be found by multiplying the impurity scattering time by the ratio of the surviving defects and the total number of atoms,

$$\frac{1}{\tau_{\mathrm{imp}}^{n_{\mathrm{defect}}}} = \frac{1}{\tau_{\mathrm{imp}}} \times \frac{n_{\mathrm{surviving}}}{n_{\mathrm{total}}}. \tag{42}$$

This ratio is close to the definition of the displacement per atom (DPA) used to predict the damage a material will receive in operation. There are some hurdles in comparing the model results with experimental data at this stage. DPA is usually calculated as the number of FP divided by the total number of atoms,

$$DPA = \frac{n_{\mathrm{FP}}}{n_{\mathrm{total}}} \tag{43}$$

this does not show how many surviving vacancy and interstitial are present; it just estimates the number of atoms that were displaced. Hence, it cannot be used directly to predict the surviving Frenkel defects.

Frenkel defects are the most basic type of defect produced during irradiation damage, and these tend to mostly recombine during the recombination phase, forming larger defect clusters, i.e. voids and dislocations, or annihilating. Additionally, due to the irradiation, transmuted elements (i.e. Re in W) can form, as well as He bubbles, and formation of hydrides. All these defects, will have different effects on

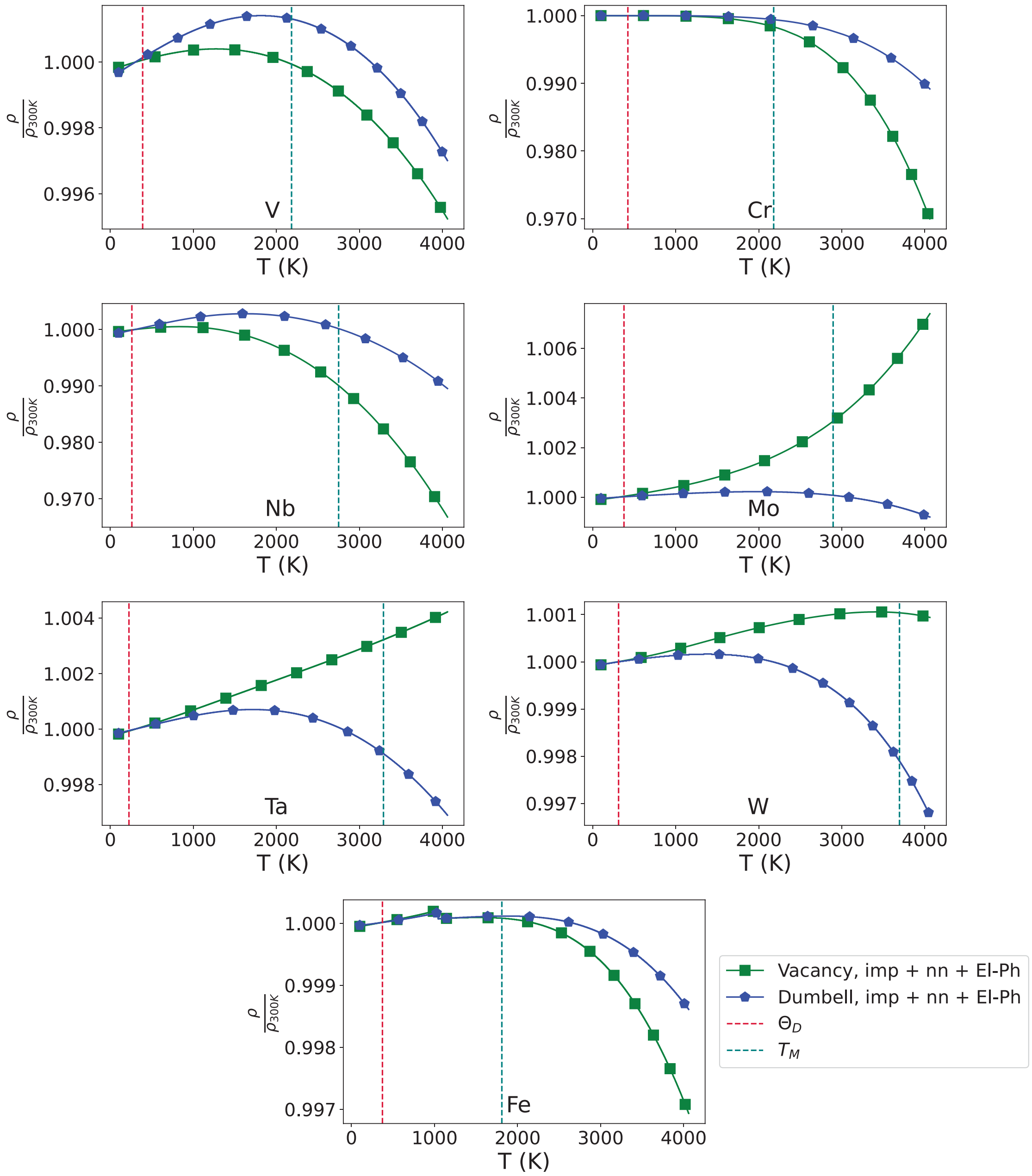

Figure 7. Ratio of the resistivity and the resistivity at 300 K of Frenkel defects in BCC transition metals. The labels specify what contribution is considered in each; 'imp' is the Frenkel defect, 'nn' is the contribution from the nearest-neighbour limit, and 'El-Ph' is the electron–phonon contribution, where the *s*-electron to *d* band corrections have been included.

the electron scattering times than the individual vacancy and interstitial. Which means that directly comparing the results with experimental data will give results that are a few orders of magnitude different, depending on what defects formed in the irradiated sample.

Echols *et al* have provided an in-depth study of the resistivity measurements at various DPAs for irradiated W that can be used to compare with this model. A plot of the DPA vs resistivity is shown in figure 9. The standard results from the model are around 2 orders of magnitude smaller than the experimental results. This is to be expected as in an actual irradiated sample the resistivity would be primarily arising from dislocation, voids, grain boundaries, transmutation impurities, He, and H impurities. The FPs would play a smaller role in the total resistivity. Additionally, the measurements from Echols *et al* include measurements at different orientations, and irradiation temperatures [4], these will also have an effect on the resistivity. Figure 3 showcases how the potential changes from the [100] direction compared to the [111] direction, this will then change the electron-impurity scattering time, and thus the resistivity. Irradiation at different temperatures will also produce different defect clusters, and this will also then affect the resistivity.

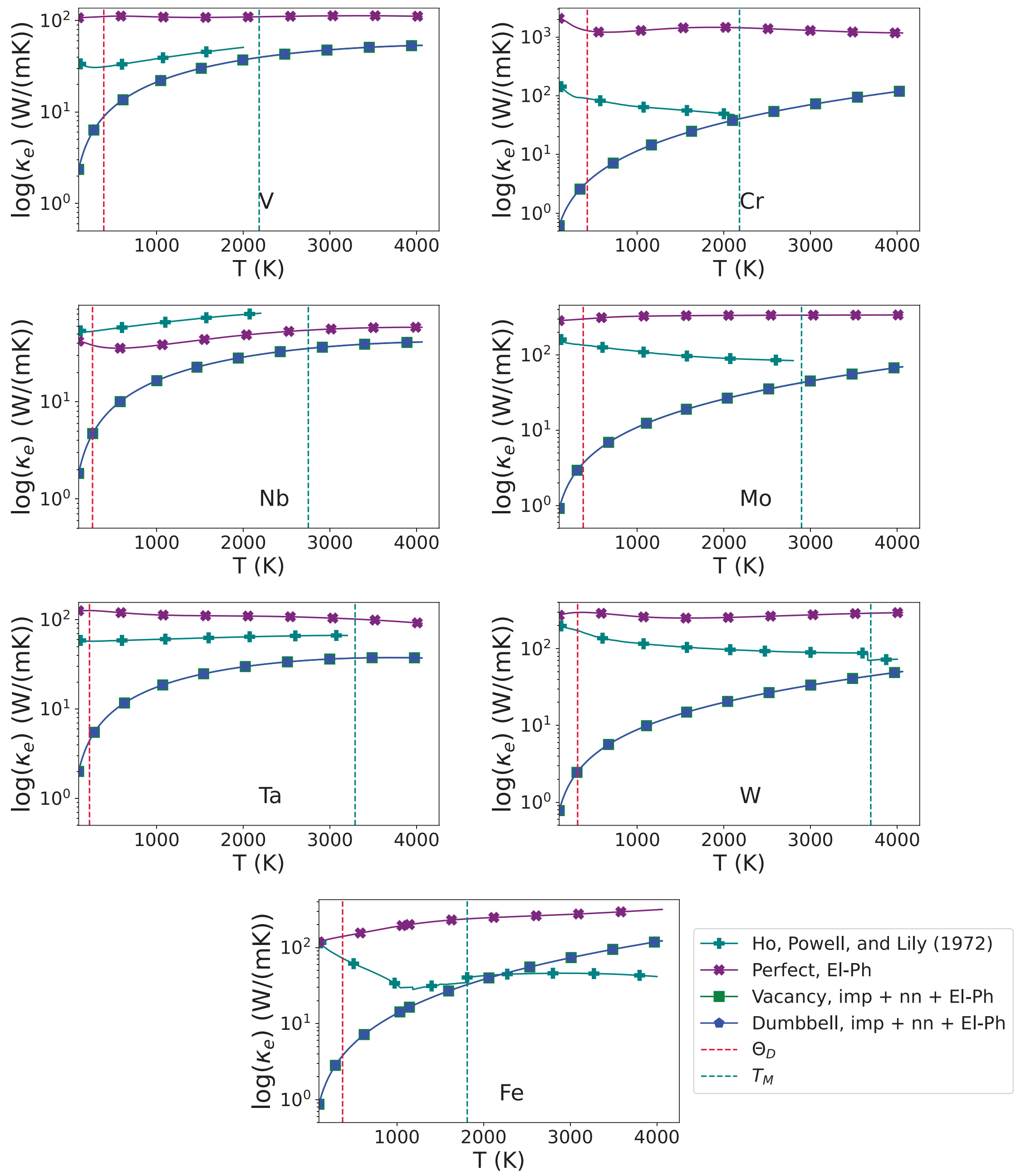

Figure 8. Thermal conductivity Frenkel defects in BCC transition metals. The labels specify what contribution is considered in each; 'imp' is the Frenkel defect, 'nn' is the contribution from the nearest-neighbour limit, and 'El-Ph' is the electron–phonon contribution with the corrections from the tetrahedron with Blöch corrections smearing with $\Delta E = 0.1$ eV. By default, they include the correction factors, except for the perfect cell. The experimental values are from Ho, Powell, and Lily [45].

6. Discussion

Fermi velocity was calculated by integrating over the Fermi surface, which meant that it required high accuracy Fermi surfaces. This was achieved by using a large K-mesh, and using a marching cube algorithm to further interpolate the surface. The results were compared with the work from Mason [2], and it showed that for Nb, Ta, and Cr the results were close, but not for the other elements. This is most likely due to the differences in the chosen potentials, and the number of valence electrons, between this work and the ones chosen by Mason. However, W Fermi velocity closely matched with experimental data by Medjanik *et al* [35], thus suggesting that it is fundamental to include semi-core electrons to obtain highly accurate Fermi surfaces. The effective mass is very susceptible to the band structure and its curvature, hence only values between $-k_B T_M < \epsilon_F < k_B T_M$ were used.

The electron heat capacity was successfully calculated by using the Fermi–Dirac function to smear the electron temperatures. As the system's energy is dependent on the electronic temperature, by double

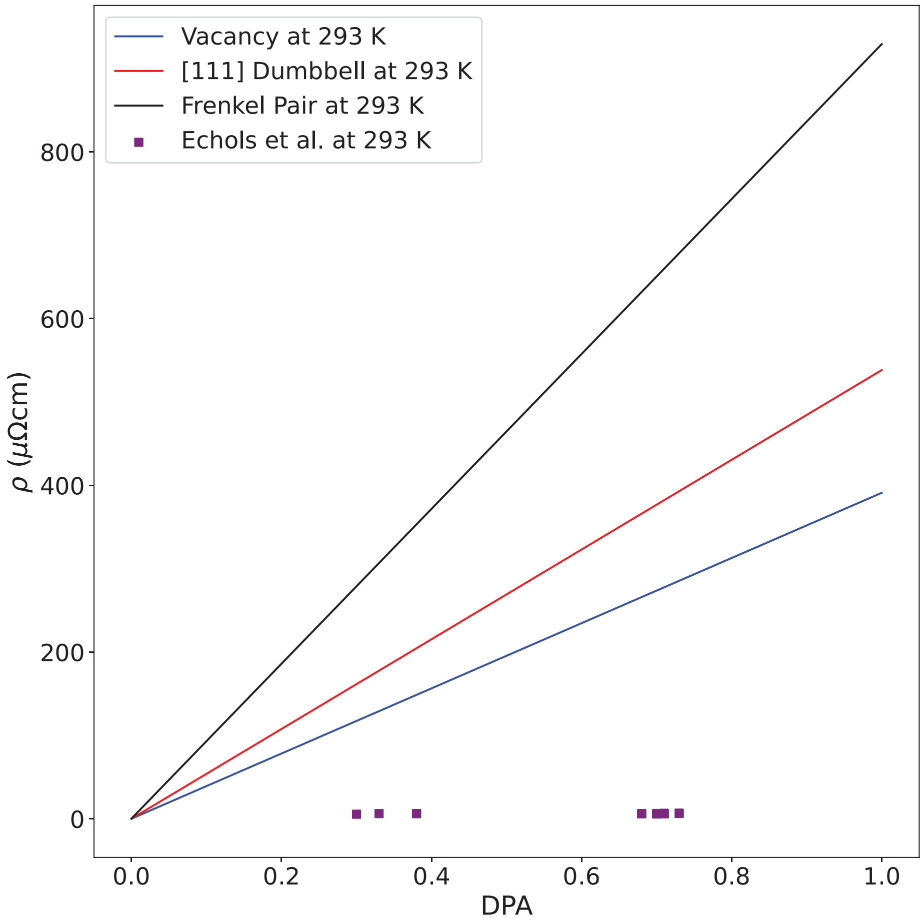

Figure 9. Resistivity of FP as a function of DPA in W. Compared with the experimental values are from Echols *et al* [4].

differentiating the energy in respect to temperature, the electronic thermal capacity was found. This was in the range of 10^{-6}, to 10^{-4} eV K−1, which is to be expected as phonons dominate the contribution to the heat capacity. In group V BCC transition metals the Sommerfeld and Free electron gas approximation are very similar, and the calculated heat capacity closely matches with the approximation at low temperatures, but it diverges at higher temperatures. Meanwhile, the Free electron gas approximation for the Group VI BCC transition metals is close to the Sommerfeld approximation at lower temperatures. The exception being Cr, which diverges at higher temperatures, most likely due to the anti-ferromagnetic moments that were included in the First principle calculations. Finally, the c_e calculated for Fe starts lower than the approximations, but starts to converge towards the Free electron approximation and the experimental result at higher temperatures. The electronic heat capacity does not fully match with the experimental data from Tari [37] in Group V, while in Group VI the results are quite close. For Cr and Fe, this is most likely due to presence of the magnetic moments. The experimental values are for low-temperature electronic heat capacity, which was then extrapolated at higher temperatures, this extrapolation might mean that some factors have not been considered which lead to the small deviations seen when comparing the experimental values to the ones calculated in this work. However, they are in the same order of magnitude and can therefore be used.

The electron-impurity scattering probability relied on finding the perturbation potential caused by the presence of defects, be it vacancy, dumbbell, or crowdion. This was achieved by performing various supercell calculations. Firstly, the defect formation energies were validated against literature data to ensure that the defects had properly formed. Then, using self-consistent calculations, the potential energy in each cell was found. This allowed to find the energy differences between the pure and the defect structure, from which the perturbation potential was extracted. The initial validation of the scattering probability was done calculating the resistivities values and comparing them with literature data. The data ended up being in the same magnitude, but not all the elements matched with the reference data. This is due to the Frenkel pair reference data being adopted values by the authors [44], and furthermore the resistivities from this work are at 0 K. However, this is enough to assume that the method to calculate the electron scattering probabilities is valid. The crowdion results were underestimated because crowdions are a 1-dimensional defect, and the current method to extract the perturbation potential only would work for 0 dimensional defects, like vacancies and dumbbells. The thermal conductivity of the defects is much lower than the experimental ones at 300 K. There are a few reasons for this; the experimental values are for the total electron thermal conductivity, which would also include the electron–phonon and electron–electron contribution. Then, there is a very high defect concentration of 1 defect for every 250 atoms. Which means that the results are giving the results not for the bulk, but close to the defect.

The electron–phonon scattering time was calculated from the Kaganov model [46] using the temperature dependent electron–phonon coupling term by Lin [47]. The scattering time for W was calculated and compared with the experimental values from Hofmann *et al* [8]. The simulation results closely match with the experimental values. And, the [111] dumbbell electron–phonon scattering time is the closest to match with the experimental data, while the vacancy closely matches with the electron–phonon time from the primitive perfect cell. All the simulation results converge with the supercell scattering time at higher temperatures, while the dumbbell increases first, and then it decreases and crosses from being the lowest scattering time at low temperatures to being the highest at high temperatures. The correction factors from the Mott model were used and applied to the electron–phonon contribution for both the resistivity and thermal conductivity. From the results, the Mott correction factors are extremely correlated to the values of the density of states at Fermi energy, where small changes in the value caused by a change in DOS smearing method or energy mesh would lead to entirely different behaviours. The number of atoms also seem to have an effect on the DOS, which will affect the correction factors. Overall, at higher temperatures, the resistivity decreases across the BCC transition metals, except in Ta and Mo where the vacancy resistivity increased. Whereas, the electron thermal conductivity increased as a function of temperature. The perfect electron–phonon thermal conductivity with no correction factors is close to the experimental values, but it is an overestimate (except in Nb). The lack of the e–*e contribution is evident, these contributions would improve the results. Additionally, the thermal conductivity of the Frenkel defects increases towards the experimental one close to the melting point of the material. The resistivity and thermal conductivity results are not the values of the bulk system, but rather show the localized effect of the defect in their surroundings, which is why the electron-impurity contribution dominates the results.

A case study was performed to understand how more realistic defect concentrations would compare with experimental data. The resistivity data for W provided by Echols *et al* [4] for various DPA was compared with the results of the resistivity calculated for increasing DPA from the model in this work. Specifically, the case for the Frenkel pair, and the individual defects were compared with the experimental data. The results from the Frenkel defects over-predict the experimental resistivity. This is because in an irradiation run the FP will be recombining, and hence using the DPA is not a good prediction of how many stable FPs will be present in the system. Additionally, an irradiated sample will also have grain boundaries, dislocations, voids, He, H, and transmutation defects (depending on the type of irradiation). These will also affect the resistivity, and hence relying solely on FPs to predict the resistivity of the irradiated sample would be erroneous. This is a weakness of the model; however, the model also allows for building up the knowledge of the scattering time for the individual defects, making the model more complete and reliable.

7. Conclusion

In conclusion, this work presented a simple method to calculate the thermal conductivity and resistivities of FP in BCC transition metals. This was done by,

(i) the Fermi velocity, effective mass, and electronic heat capacity were calculated from first principle simulations.

(ii) Then a method to calculate the electron-impurity scattering time for 0 dimensional defects is presented. This relies on finding the perturbation potential from the differences in potential energy caused by the presence of the defect. This gave good results that match with experimental data or are in the same order of magnitude.

(iii) The model is extended to the first temperature approximation by including the electron–phonon contribution. Additionally, the correction factors for the scattering from *s*-electrons to the *d*-band from the Mott model are included in the electron–phonon contribution. The inclusion of the electron–phonon scattering time is not as evident due to high defect concentration in the structures, but it does have an effect on the results. The corrections factor mostly decrease the resistivity while increasing the thermal conductivity.

Finally, this method can be extended to calculate the thermal and electrical properties of irradiated BCC transition metals that have elemental impurities due to transmutations, alloys system, like high entropy alloys (HEA). In HEAs, there is an additional source of scattering coming from the random atomic position of the elements, which leads to an 'electron-disorder' scattering contribution. The electron-impurity methodology developed in this work can be used to calculate the 'electron-disorder', and since a HEA is mainly disordered, this implies that the electron-disorder contribution will be the dominating one and the approximation used in this model would be effective. However, this would require additional and thorough investigation with different kinds of HEA to confirm its accuracy.

The current devised model only applies to point defects; defects like dislocations, vacancy clusters, and voids would require a further investigation of the spatial correlation of the potential. With some considerations, the model could be expanded to study the effects of dislocations.

This model brings us closer to a full *Ab-Initio* picture of the degradation of thermal and electrical properties in transition metals for nuclear applications.

Acknowledgments

We would like to thank D Mason for the very insightful and valuable discussions. This work is supported by the Centre of Doctoral Training in Topological Design (funded by the Engineering and Physical Sciences Research Council (EPSRC) [Grant Number EP/S02297X/1]) and the University of Birmingham. The computations described in this paper were performed using the University of Birmingham's BlueBEAR HPC service, which provides a High-Performance Computing service to the University's research community. See www.birmingham.ac.uk/bear for more details. DNM would like to acknowledge funding from the EPSRC Energy Programme [Grant Number EP/W006839/1]. BC would like to thank the support from the UKRI Future Leaders Fellowship (MR/W007967/1).

Data availability statement

The data that support the findings of this study are openly available at the following URL/DOI: https://doi.org/10.5281/zenodo.19592795 [59].

Author contributions

J Singh 0009-0002-2357-8553
Conceptualization (lead), Data curation (equal), Formal analysis (equal), Investigation (equal), Methodology (equal), Resources (equal), Software (equal), Validation (equal), Visualization (lead), Writing – original draft (lead), Writing – review & editing (equal)

D Nguyen-Manh 0000-0001-6061-9946
Conceptualization (lead), Data curation (equal), Formal analysis (equal), Funding acquisition (supporting), Investigation (equal), Methodology (equal), Project administration (equal), Resources (supporting), Software (supporting), Supervision (lead), Validation (lead), Visualization (supporting), Writing – original draft (equal), Writing – review & editing (lead)

A Mottura 0000-0002-6020-8597
Project administration (supporting), Supervision (supporting), Writing – review & editing (supporting)

B Cai 0000-0001-7355-0220
Funding acquisition (lead), Project administration (lead), Supervision (equal), Writing – review & editing (supporting)

Appendix. Perturbation potential extraction

To analyse the potential, the number of slices has to be determined. The minimum number of suggested slices in any direction corresponds to the grid points, $NGX \times NGY \times NGZ$, determined by VASP, these can be found in the LOCPOT or in the OUTCAR files. The grid of $NGX \times NGY \times NGZ$, is determined by VASP depending on the number of plane-wave cut-offs; however, they can also be set manually if needed. Figure A1 shows the potential of the perfect cell of W, from this it can be deduced that the potential obtained from slicing should give a periodical potential.

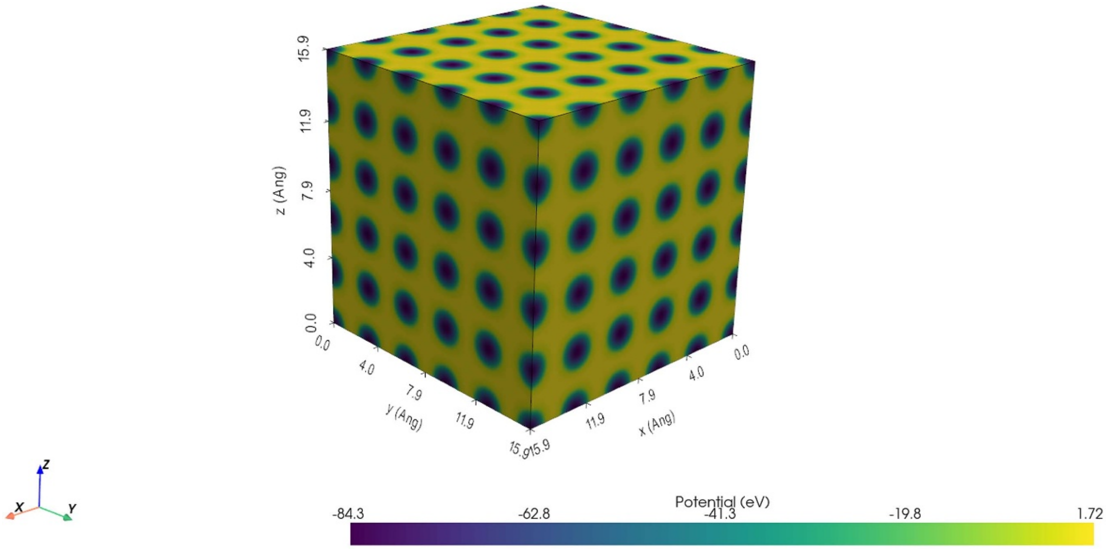

Figure A1. Potential of W for the perfect structure. Visualized using PyVista [38]. The dark spots represent where the atoms can be found, while the area in yellow shows the 'empty' space between atoms.

To better show why this is the case, figure A2 shows how changing the number of slices affects the quality of the output potential. From the figure, 10 slices are not enough to correctly construct a periodic potential, and most of the information of the periodicity of the potential is lost. With 100 slices, the potential is a lot more well-defined, but the potential around the maxima and the minima is still quite rough. However, with NGX slices, which for W is 256 slices, the potential is both well-defined and smooth around the maxima and minima. It becomes clear from the images, that the number of slices can also be used to determine the resolution of the potential. In terms of this work, 1048 slices were performed in each of the x, y, z directions, while 2048 were performed for the [111] direction were chosen to provide a resolution of ≈ 0.01 Å across all BCC transition metals for ease of comparison.

The number of slices determines the resolution of the cell, but to determine the perturbation potential, the analysis has to be performed over the difference in the potential energies of the perfect cell and the defect. An example is given in figure A3 for the perturbation potential from the [111] dumbbell in W. The difference is given by,

$$E_{\mathrm{diff}} = E_{\mathrm{perf}} - E_{\mathrm{imp}} \tag{A.1}$$

where E_{perf} is the potential energy from the perfect structure, and the E_{imp} is the potential energy from the impurity.

The perturbation potential is extracted from the region where the defect is situated. The region of interest (ROI) is defined as the following,

$$P - \frac{a_0\sqrt{3}}{2} \leqslant P \leqslant P + \frac{a_0\sqrt{3}}{2} \tag{A.2}$$

where $P(x, y, z)$ is the position of the perfect atom that was substituted by the defect, which corresponds to the atom at the centre of the supercell, which is also the central atom of the [111] string. The $a_0\sqrt{3}/2$ corresponds to the nearest-neighbour distance in BCC transition metals. Figure A3 showcases the ROI, by delimiting it with black lines. In the figure, the position of the perfect atom is shown by a dashed

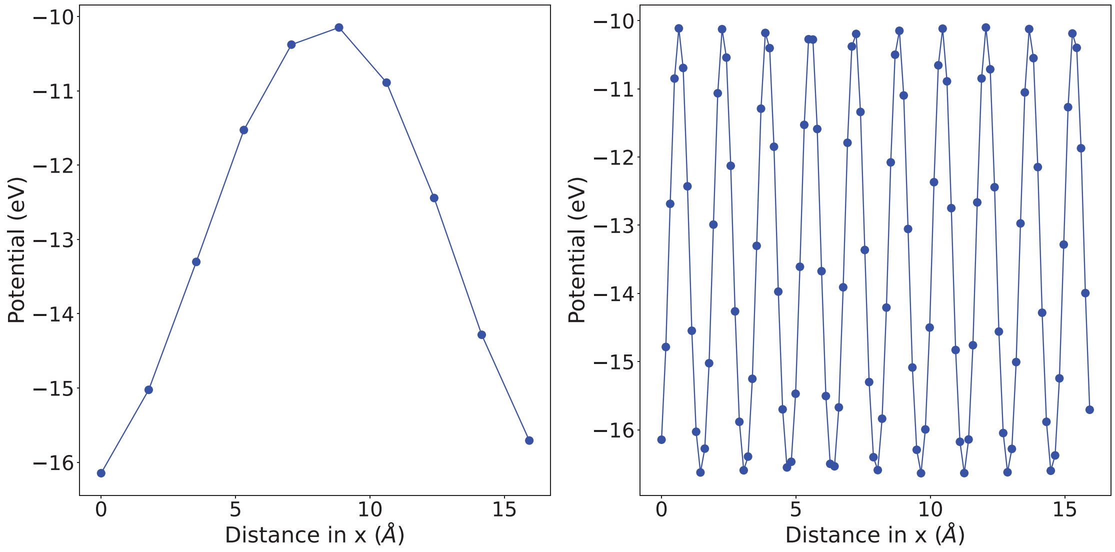

(a) 10 slices in the x-direction (b) 100 slices in the x-direction

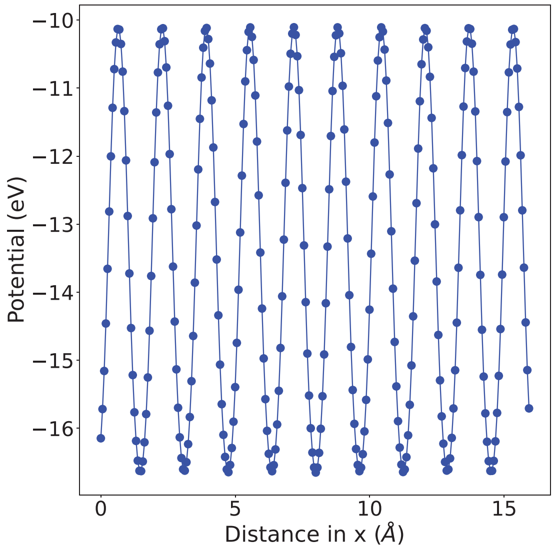

(c) NGX $(=256)$ slices in the x-direction

Figure A2. Determining the minimum number of slices needed to obtain a continuous, well-defined potential. Each blue dot corresponds to a slice. The potential is from the perfect structure of W in the x-direction.

black line, whereas the red dashed lines represent the atoms of the [111] dumbbell. The perturbation potential is found by averaging the difference of the maxima and the minima in the ROI, and dividing the result by two. The division by two is done because the potential difference is the result of the overlap of two different structures. This process is shown in figure 3 in the main text, and it is calculated as,

$$U_{\text{pertubation}} = \frac{\overline{\max\left(E_{\text{diff}}\left(P\right)\right) - \min\left(E_{\text{diff}}\left(P\right)\right)}}{2} \qquad \text{for } P - \tfrac{a_0\sqrt{3}}{2} \leqslant P \leqslant P + \tfrac{a_0\sqrt{3}}{2} \tag{A.3}$$

This equation is used to calculate the perturbation potential for the defects show in table A1.

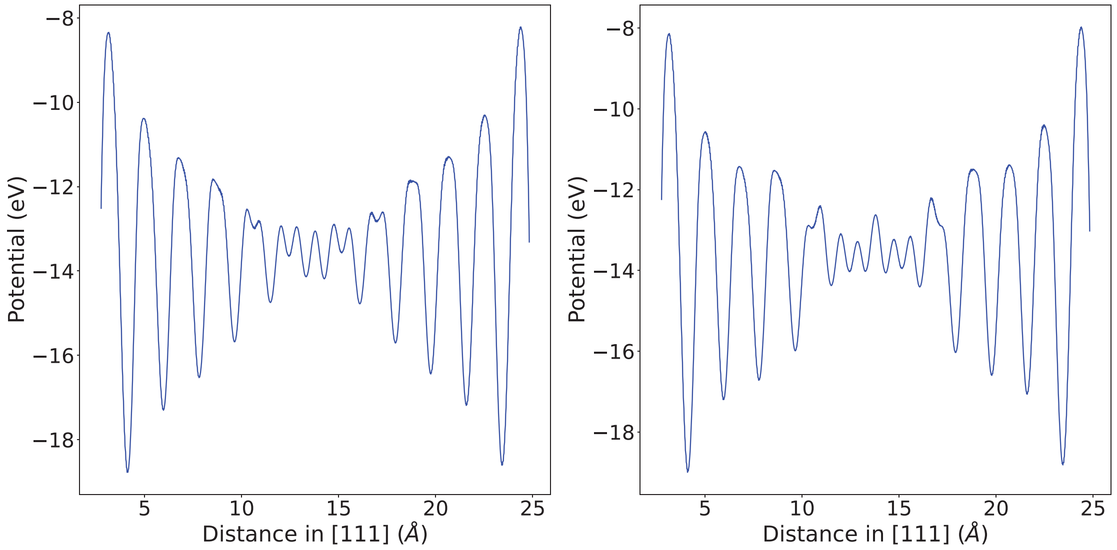

(a) Potential of the perfect structure

(b) Potential of the dumbbell structure

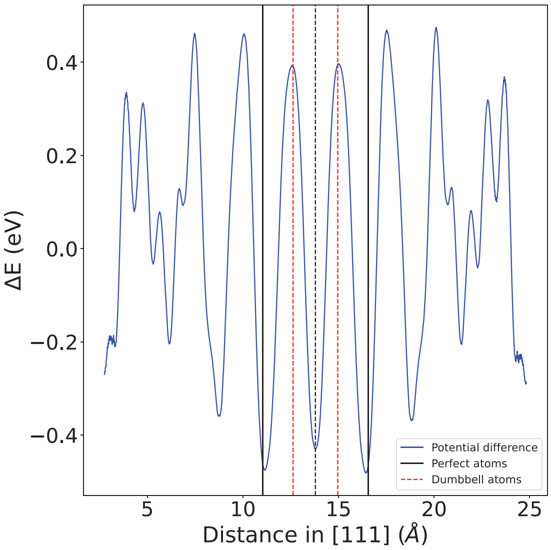

(c) Perturbation potential for the [111] dumbbell.

Figure A3. Potential difference between the perfect and [111] dumbbell structures.

Table A1. Perturbation potentials of Frenkel defects in BCC transition metals.

	Potential (eV)		
Element	U_{vac}	U_{db}	U_{cd}
V	−0.329	0.267	0.214
Nb	−0.372	0.329	0.210
Ta	−0.368	0.361	0.137
Cr[13]	−0.575	0.537	0.187
Mo	−0.447	0.475	0.123
W	−0.424	0.437	0.105
Fe[14]	−0.571	0.746	/

[13] Spin polarized anti-ferromagnetic.

[14] Spin polarized ferromagnetic, [110] dumbbell.

References

[1] Ashcroft N W and Mermin N D 1976 *Solid State Physics* (Saunders College Publishing)
[2] Mason D 2015 *J. Phys.: Condens. Matter* **27** 145401
[3] Was G S 2007 *Fundamentals of Radiation Materials Science: Metals and Alloys* (Springer)
[4] Echols J R, Garrison L M, Reid N, Parish C M, Hasegawa A, Bhattacharya A, Zhong W, Morrall D, Lance M and Katoh Y 2023 *Acta Mater.* **257** 119025
[5] Sina H, Dai Y, Lee Y and Wohlmuther M 2024 *J. Nucl. Mater.* **601** 155324
[6] Akiyoshi M, Garrison L M, Geringer J W, Wang H, Hasegawa A, Nogami S and Katoh Y 2021 *J. Nucl. Mater.* **543** 152594
[7] Short M P, Dennett C A, Ferry S E, Yang Y, Mishra V K, Eliason J K, Vega-Flick A, Maznev A A and Nelson K A 2015 *JOM* **67** 1840–8
[8] Hofmann F, Mason D R, Eliason J K, Maznev A A, Nelson K A and Dudarev S L 2015 *Sci. Rep.* **5** 1–7
[9] Hofmann F, Short M P and Dennett C A 2019 *MRS Bull.* **44** 392–402
[10] Quintero-Bermudez R, Drescher L, Eggers V, Xiong K G and Leone S R 2025 *ACS Photonics* **12** 2097–105
[11] Dechaumphai E, Barton J L, Tesmer J R, Moon J, Wang Y, Tynan G R, Doerner R P and Chen R 2014 *J. Nucl. Mater.* **455** 56–60
[12] Cui S, Simmonds M, Qin W, Ren F, Tynan G R, Doerner R P and Chen R 2017 *J. Nucl. Mater.* **486** 267–73
[13] Koo D, Park J, Jung M, Park S, Na H S, Kim W, Park H S and So H 2025 *Case Stud. Therm. Eng.* **74** 106888
[14] Carbogno C, Ramprasad R and Scheffler M 2017 *Phys. Rev. Lett.* **118** 175901
[15] Zhang D B, Li J G, Ren Y H and Sun T 2023 *Phys. Rev. B* **108** 104307
[16] Wirnsberger P, Frenkel D and Dellago C 2015 *J. Chem. Phys.* **143** 124104
[17] Mason D R, Reza A, Granberg F and Hofmann F 2021 *Phys. Rev. Mater.* **5** 125407
[18] Kittel C 2005 *Introduction to Solid State Physics* 8th edn (Wiley)
[19] Madsen G K, Carrete J and Verstraete M J 2018 *Comput. Phys. Commun.* **231** 140–5
[20] Smirnov N A 2022 *Phys. Rev. B* **106** 024109
[21] Claes R, Brunin G, Giantomassi M, Rignanese G M and Hautier G 2022 *Phys. Rev. B* **106** 094302
[22] Jayaraj A, Siloi I, Fornari M and Nardelli M B 2022 *Sci. Rep.* **12** 1–12
[23] Mott N F and Jones H 1936 *The Theory of the Properties of Metals and Alloys* (Oxford University Press)
[24] Kresse G and Furthmüller J 1996 *Comput. Mater. Sci.* **6** 15–50
[25] Kresse G and Hafner J 1993 *Phys. Rev. B* **47** 558–61
[26] Kresse G and Furthmüller J 1996 *Phys. Rev. B* **54** 11169–86
[27] Hinuma Y, Pizzi G, Kumagai Y, Oba F and Tanaka I 2017 *Comput. Mater. Sci.* **128** 140–84
[28] Togo A, Shinohara K and Tanaka I 2024 *Sci. Technol. Adv. Mater.: Methods* **4** 2384822
[29] Wang V, Xu N, Liu J C, Tang G and Geng W T 2021 *Comput. Phys. Commun.* **267** 108033
[30] Fitzgerald S P and Nguyen-Manh D 2008 *Phys. Rev. Lett.* **101** 115504
[31] Rutter M J 2018 *Comput. Phys. Commun.* **225** 174–9
[32] Kokalj A 1999 *J. Mol. Graph. Model.* **17** 176–9
[33] Weinberger T 2023 py_fs Github repository (available at: https://github.com/TheoWeinberger/py_FS/)
[34] Harris C R *et al* 2020 *Nature* **585** 357–62
[35] Medjanik K *et al* 2017 *Nat. Mater.* **16** 615–21
[36] Balmer R T 2011 *Modern Engineering Thermodynamics* (*Modern Engineering Thermodynamics*) (Elsevier) pp 362–4
[37] Tari A 2003 *The Specific Heat of Matter at Low Temperatures* (published by Imperial College Press and distributed by World Scientific Publishing Co.)
[38] Sullivan C B and Kaszynski A A 2019 *J. Open Source Softw.* **4** 1450
[39] Nguyen-Manh D, Horsfield A P and Dudarev S L 2006 *Phys. Rev. B* **73** 020101
[40] Derlet P M, Nguyen-Manh D and Dudarev S L 2007 *Phys. Rev. B* **76** 054107
[41] Schultz H 1991 2.2.1 Special remarks *Atomic Defects in Metals* vol 25, ed H Ullmaier (Springer) pp 115–20
[42] Ullmaier H 1991 *Atomic Defects in Metals* vol 25 (Springer)
[43] Rasch K D, Siegel R W and Schultz H 1980 *Philos. Mag. A* **41** 91–117
[44] Broeders C H and Konobeyev A Y 2004 *J. Nucl. Mater.* **328** 197–214
[45] Ho C Y, Powell R W and Liley P E 1975 *Thermal Conductivity of the Elements : a Comprehensive Review* vol 3 (American Institute of Physics)
[46] Kaganov M, Lifshitz I and Tanatarov L 1957 *J. Exp. Theor. Phys.* **4** 173 (available at: www.jetp.ras.ru/cgi-bin/e/index/e/4/2/p173?a=list)
[47] Lin Z, Zhigilei L V and Celli V 2008 *Phys. Rev. B* **77** 075133
[48] Samsonov G V 1968 *Handbook of the Physicochemical Properties of the Elements* pp 387–446
[49] Brorson S D, Kazeroonian A, Moodera J S, Face D W, Cheng T K, Ippen E P, Dresselhaus M S and Dresselhaus G 1990 *Phys. Rev. Lett.* **64** 2172
[50] Fletcher G, Fry J L, Pattnaik P C, Papaconstantopoulos D A and Bacalis N C 1988 *Phys. Rev. B* **37** 4944–9
[51] Al-Lehaibi A, Swihart J C, Butler W H and Pinski F J 1987 *Phys. Rev. B* **36** 4103
[52] Mazin I I, Savitskii E M and Uspenskii Y A 1984 *J. Phys. F: Met. Phys.* **14** 167
[53] Allen P B 1987 *Phys. Rev. B* **36** 2920–3
[54] Mott N F and Wills H H 1936 *Proc. R. Soc. London A* **153** 699–717
[55] Aisaka T and Shimizu M 1970 *J. Phys. Soc. Japan* **28** 646–54
[56] Chiu J C 1976 *Phys. Rev. B* **13** 1507
[57] Mott N F 1935 *Proc. Phys. Soc.* **47** 571–88
[58] Virtanen P *et al* 2020 *Nat. Methods* **17** 261–72
[59] Singh J, Nguyen-Manh D, Mottura A and Cai B Electronic contribution of Frenkel defects to thermal conductivity in body centred cubic transition metals from first-principles study *Zenodo* (available at: https://doi.org/10.5281/zenodo.19592795)